A Project report on

"Synthesis, characterization and Thermo luminescence studies of Yttrium Oxide (Y_2O_3) nanophosphor doped with different rare earth ions"

Submitted to

The Deputy Secretary, Regional Head,
University Grants Commission, South Western Regional Office, Bangalore- 560009.

Submitted by
B. Marappa
Assistant Professor in physics
SreeSiddaganga college of Arts, Science and Commerce for women
Tumkur, Karnataka-572102

To

Deputy Secretary, Regional Head
University Grants Commission
South Western Regional Office
Bangalore-560009

Respected Sir,

Subject: Regarding Submission of Final Report of Minor Research Project.

Reference: MRP(S)-0171/12-13/KATU008/UGC-SWRO Dated 23-09-2013

With reference to above cited subject and reference, here by I am submitting the final progress report of Minor Research project of B.Marappa entitled "**Synthesis, characterization and Thermo luminescence studies of Yttrium oxide (Y_2O_3) nanophosphor doped with different rare earth ions** .This is for your kind consideration and needful

He has completed the project work, one copy of this work is kept in our college library for student's reference and another is uploaded in college website (**www.sscwtumkur.org**).

Thanking you sir

Yours faith fully

(B.MARAPPA)Principal
Principal Investigator

Different fuel approach Auto ignition synthesis of Nano Y_2O_3 and comparative study of Structural, photo and thermo luminescence properties

1. Introduction:

Rare earth oxides (REO) have been extensively studied in recent years not only because of their unique electronic, optical, and chemical properties, but also their potential applications in various fields[1,2]. Among many REO, Y_2O_3 has been regarded as one of the more promising material for the dielectric insulator of complementary metal oxide semiconductor (CMOS) devices as consequence of its particular physical properties such as wide energy gap (5.5 eV) relatively high dielectric constant and good thermal stability (up to 2325 ^oC). Furthermore, Y_2O_3 is an important material for optical applications because of its ability to be a host material for rare earth atoms [3,4]. For instant as the main and unsurpassed red emitting materials in fluorescent lamps and flat panel devices,[5-7] Y_2O_3 : Eu^{3+} phosphors inevitably gather more attention because of its good luminescent characteristic, acceptable atmospheric stability, reduced degradation under applied voltages, and the lack of hazardous constituents as opposed to sulfide phosphors.[8]

A wide variety of processes are available for the synthesis of REO. Y_2O_3powder has been reported to be synthesized by various wet chemical routes, such as, co-precipitation [9], hydrothermal [10], sol–gel [11], gas-phasecondensation[12] and solution combustion [13,14] route. With appropriate processing parameters these wet chemical processes can produce nano-size powders in narrow particle size distribution.Among the above-mentioned processes the solution combustion process is characterized by fast reaction rate and low cost. In the solution combustion route a self-sustaining exothermic redox reaction is allowed to take place in the gel that is formed on dehydrating an aqueous solution of a fuel (such as, polycarboxilic acid) and an oxidant (metal nitrate). The powder characteristics like crystallite size, surface area, extent and nature (hard or soft) of agglomeration

areprimarily governed by enthalpy or flame temperature generated during combustion, which itself is dependent onnature of the fuel, fuel-to-oxidant ratio and amount of evolved gases [15].

Y_2O_3-based powders have been previously synthesized by a combustion synthesis process using various fuels. It has been noted that the choice of fuel alters the exothermicity and amount of evolved gases during the combustion process which have a strong influence on the properties of the product [16]. The fuels so far employed in the combustion synthesis of Y_2O_3-based powders are glycine [17], citric acid [18], urea [19], oxalyldihydrazide[20], carbohydrazide[21], etc.

One of the organic complexing agents EDTA is known to act as a complexing agent for a number of metal ions as it has amine groups. Such molecules can effectively complex metal ions of varying size that helps in achieving homogeneity among the constituents. On the other hand EDTA can also serve as a fuel in the combustion reaction. But its use as fuel in solution combustion reaction is not extensively studied. In the present work, we prepared nano Y_2O_3 powder by combustion technique using two different fuels viz EDTA and Na_2-EDTA. The combustion synthesized powers are characterized by PXRD, FTIR, and SEM. The variation in the power characteristics obtained for different fuels are logically discussed. Dependence of photo and thermo luminescence properties of the combustion derived products is also discussed.

2. Experimental

Chemicals

Analargrade yttrium oxide (Y_2O_3: 99.99%, CDH Ltd.),nitric acid (HNO_3: 99.99%, Merk Ltd.) EDTA ($C_{10}H_{16}N_2O_8$: 99.99%, Merk Ltd.)and Na_2-EDTA ($C_{10}H_{14}N_2O_8Na_2$: 99.99%, Merk Ltd.)were used as starting materials for the preparation of Y_2O_3nanoparticles. The entire chemicals were used without further purification.

Synthesis:

Yttrium oxide was dissolved in 1:1 nitric acid and heated on a sand bath at 80 ° C to get transparent high viscous yttrium nitrate gel and excess nitric acid was evaporated. The EDTA was dissolved in deionized water and the solution was subsequently dropped into the yttriumnitrate solution and continuous stirring was done to ensure the homogeneous solution. The Petri dish containing the homogeneous mixture of metal nitrates yttrium nitrate, and EDTA was placed in a pre-heated muffle furnace maintained at 500 ± 10 ◦C. Initially, the solution boiled and underwent dehydration, followed by decomposition with the evolution of large amounts of gases (oxides of carbon, nitrogen). Then, spontaneous smoldering type combustion with enormous swelling occurs, producing foamy and voluminous Y_2O_3. Same procedure was followed in preparation of Y_2O_3 with disodium salt of EDTA as fuel.The theoretical equations (F/O = 1.0) for the formation of Y_2O_3 nanoparticles using differentfuels can be represented by the following reactions:

EDTA:$8Y(NO_3)_3+3C_{10}H_{16}N_2O_8 \rightarrow$

$4Y_2O_3+30CO_2+15N_2+24H_2O,$ ~13 moles of gases/mol of Y_2O_3

Na_2-EDTA:$10Y(NO_3)_3+3C_{10}H_{14}N_2O_8Na_2 \rightarrow$

$5Y_2O_3+NaNO_3+30CO_2+15N_2+21H_2O,$ ~17 moles of gases/mol of Y_2O_3

Characterization

The phase purity and the crystallinity of the nanophosphors were examined by powder X-ray diffractometer (PANalytical X′Pert Pro) using CuK_α(1.541Å) radiation with a nickel filter. The surface morphology of the product was examined by Scanning Electron Microscopy (SEM) (JEOL JSM 840A).A Quanta Chrome Corporation NOVA 1000 gas sorption analyzer was used to find the surface area of the powder samples. Transmission Electron Microscopy (TEM) analysis was performed on a Hitachi H-8100 (accelerating voltage up to 200 kV, LaB_6 filament) equipped with

EDS (Kevex Sigma TM Quasar, USA).The FT-IR studies were performed on a Perkin Elmer Spectrometer (Spectrum 1000) with KBr pellets. The UV-VIS absorption of the samples was recorded on SL 159 ELICO UV - VIS Spectrophotometer. The photoluminescence (PL) measurements were performed on a JobinYvonspectrofluorimeter (Fluorolog–3) equipped with a 450-W xenon lamp as an excitation source. TL measurements were carried out at room temperature using Nucleonix TL reader, using UV- irradiation as excitation with irradiation time in the range 20-140 min.

Fig. 1a and b represents the XRD patterns of the products obtained using EDTA and Na_2-EDTA fuels respectively. XRD patterns for both the samples show peaks corresponding to all the planes of standard cubic phase Y_2O_3 (JCPDS 70-0134).The diffraction pattern for EDTA Y_2O_3shows broad and unresolved XRD lineswhereasXRDpattern for Na_2-EDTA Y_2O_3 sample show crystalline and well resolved peaks. This difference in crystallinity of samples with changing the fuel may be due to the difference in the number of moles of gases evolved during combustion.

The average crystallite size (D) of Y_2O_3 samples for different fuels are estimated from the full width at half maximum (FWHM) of the (222) diffraction peak of the powders, using Scherrer formula.[22]From the observed XRD patterns, it is evident that tensile lattice strainisdifferent for samples prepared using different fuels.

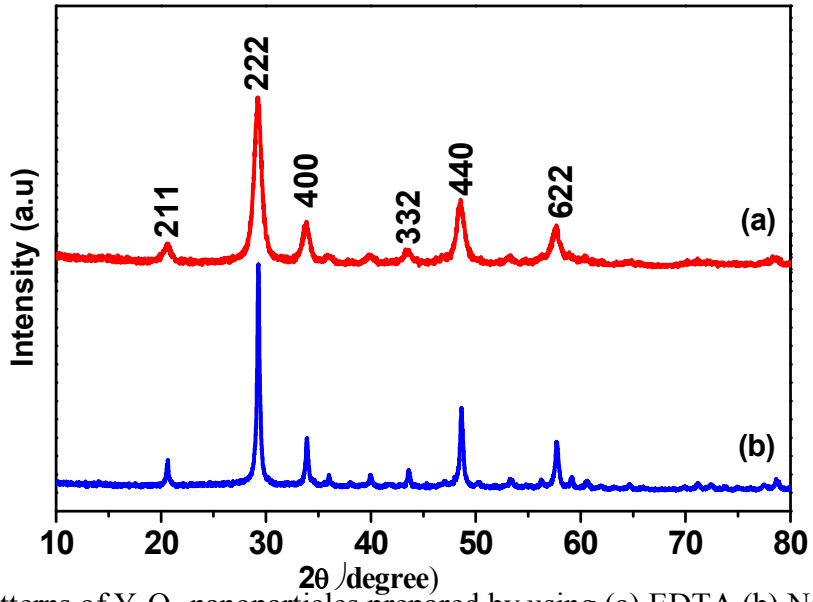

Fig.1. PXRD patterns of Y_2O_3 nanoparticles prepared by using (a) EDTA (b) Na_2-EDTA fuels

To quantify this correlation, we followed a method suggested by Williamson and Hall (W–H) [23]. The W-H method is applicable in cases where the domain effect and lattice deformation are both simultaneously operative and their resultant effects give rise to the observed FWHM (β) in the XRD patterns. βis the sum of β1(grain size dependent broadening) and β2 (lattice distortion dependent broadening). This relation assumes a negligibly small instrumental contribution compared to the sample-dependent broadening. W–H equation may be expressed in the form

$$\boldsymbol{\beta cos\,\theta = \varepsilon(4\,sin\theta) + \frac{\lambda}{D}} \quad \text{.....(1)}$$

where β (FWHM in radian), ε is the strain developed and D is the grain size. The equation represents a straight line between 4 sin θ (X-axis) and β cosθ (Y-axis), where 2θ is the Bragg angle corresponding to XRD peaks. The slope of line gives the strain (ε) and intercept (λ/D) of this line on the Y-axis gives grain size (D). Fig.2 shows W-H plot for Y_2O_3nanopowders prepared with different fuels.

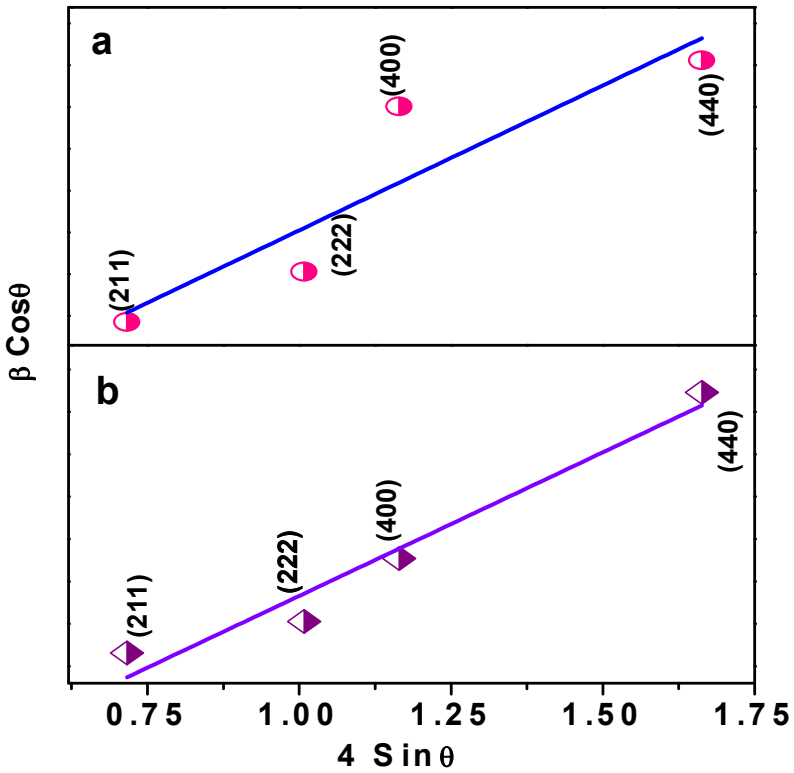

Fig.2. W−H plots of Y_2O_3 nanoparticles prepared by using (a) EDTA (b) Na_2-EDTA fuels

The crystallite sizes of the powders as determined from Scherrer's formula and W-H method are summarized in Table 1. Lowest crystallite size is observed for sample prepared using EDTA fuel due to amorphous nature of the product. It is interesting to notice that crystallinity and crystallite size increases for sample prepared using Na_2-EDTA fuel. This is attributed to sodium ions present in the Na_2-EDTA sample. The sodium ions present in the fuel may react with NO_3^- of the precursor and form $NaNO_3$, this act as flux and helps in homogeneous mixing of reactants and uniform distribution of reactant ions that form chelate with the fuel. This results in the uniform and homogeneous combustion reaction, which in turn aid in improved crystallization.

Table1. Estimated Crystallite Size and Strain ofY_2O_3 nanoparticles prepared by different fuels

System	Crystallite Size (nm)		Band Gap (eV)	Strain ($X10^{-4}$)
	Scherer's	W-H plots		
EDTA-Y_2O_3	10 nm	11 nm	4.88	14.370
Na_2EDTA-Y_2O_3	30.159nm	32 nm	5.2	5.029

From the X-ray line broadening data, we notice that the diffraction peaks become broader for sample prepared using EDTA. The observed increase in FWHM of XRD peaks in this sample is attributed to reduced crystallinity or formation of smaller crystallites in these samples.This is attributed to the fact that the solubility of EDTA is less compared to Na_2-EDTA fuel therefore this results in less homogeneous combustion with reducedflame temperature. In addition to this the number of moles of gases evolved is more for EDTA fuel than Na_2-EDTA fuel.The reduced temperature coupled with increased gas emission reduces the possibility of local sintering among the primary crystallites, thereby reducing the crystallite growth.

The Rietveld refinement is amethod in which various parameters of the XRD pattern(FWHM of peaks, asymmetry of peaks, peak shifts, etc.) can beused to estimate the crystal structure of the material under study. in present study Rietveld method was applied mainly for the purpose of evaluating unit cell parameters of the samples and the refinement done on theY_2O_3nanoparticles for EDTA acid and Na_2-EDTA fuels are shown in (Fig. 3).

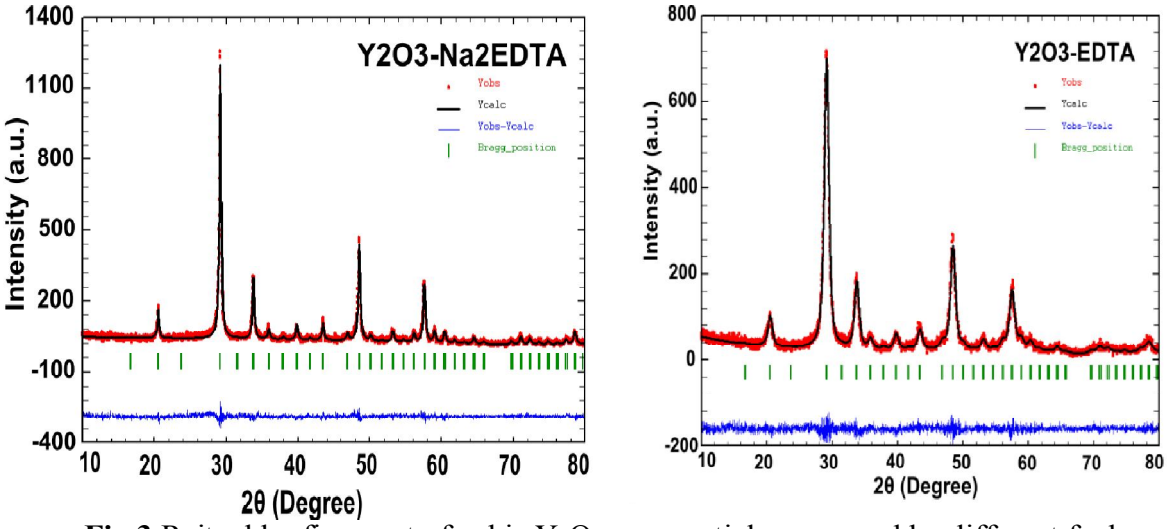

Fig.3. Reitveld refinement of cubic Y_2O_3 nanoparticles prepared by different fuels.

In our work, the Rietveld refinement was done using FULLPROF program [24]. We utilize the psedo-voigt function in order to fit the several parameters to the data point: one scale factor, one zero shifting, four back ground, three cell parameters, five shape and width of the peaks, one global thermal factors and two asymmetric factors. The final refinement analysis shows that the experimental and calculated PXRD patterns obtained by the Rietveld refinement are in good agreement with each other.The packing diagram of corresponding Y_2O_3 nanoparticles for Na_2-EDTA fuel after Rietveld refinement is shown in Fig. 4.

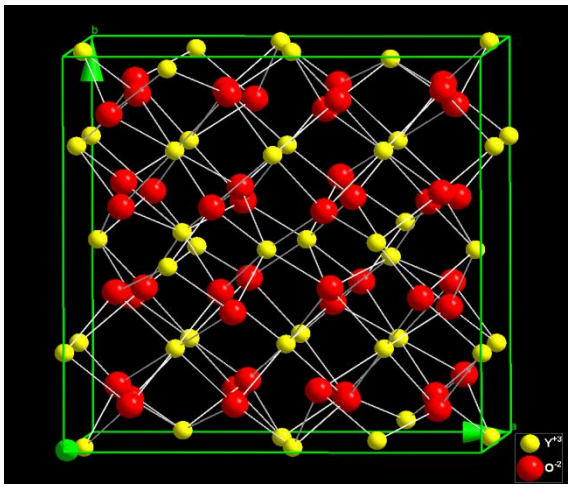

Fig.4.Packing diagram of cubic Y_2O_3 prepared by Na_2-EDTA fuels.

The refined parameters such as occupancy and atomic functional positions of the Y_2O_3 nanoparticles are summarized in Table 2. The fitting parameters (Rp, Rwp and χ^2) indicate a good agreement between the refined and observed PXRD patterns for the Y_2O_3 nanoparticles.

Table 2. Rietveld refined structural parameters of cubic Y_2O_3 nanoparticles prepared using EDTA and Na_2-EDTA as fuels

Parameters	Fuel	
	EDTA	Na_2-EDTA
Crystal system	Cubic	Cubic
Space group	Ia3-206	Ia3-206
Lattice parameter	10.632 (4)Å	10.612(8) Å
Y1	8b	8b
x	-0.0304(3)	-0.0306(3)
y	0.0000	0.0000
z	0.2500	0.2500
Y2	24d	24d
x	0.2500	0.2500
y	0.2500	0.2500
z	0.2500	0.2500
O1	48e	48e
x	0.3911(2)	0.3975(2)
y	0.1563(2)	0.1515(2)
z	0.3836(2)	0.3857(2)
R-factors		
R_p	9.0	10.1
R_{wp}	12.4	13.6
R_{Bragg}	2.32	5.92
RF	2.30	4.60
χ^2	0.804	0.902

The phase formation and purity of the products were further confirmedby FTIR spectroscopy and results are shown in Fig. 5(a) and (b). The strong absorption peak ~ 552 cm^{-1} is ascribed to the stretching vibration of the Y-O bond [24]. Further, the absorption bandsin the range 1400–1600 $cm^{-1}$are ascribed to CO_3^{2-} anion groupsand the absorption peak at 3445$cm^{-1}$is due to H_2O, which is typical of most of nanocrystalline materials due to absorbed moisture from the environment. It is

also worth noticing a band at ~ 2360 cm^{-1} corresponding to nitrate group (NO_3^-) that are the source of the starting materials. We found no more significant differencein FTIR spectra of the samples prepared with different fuels. As similar to PXRD results, FT-IR studies further confirms the formation of pure Y_2O_3 product with no other major impurities.

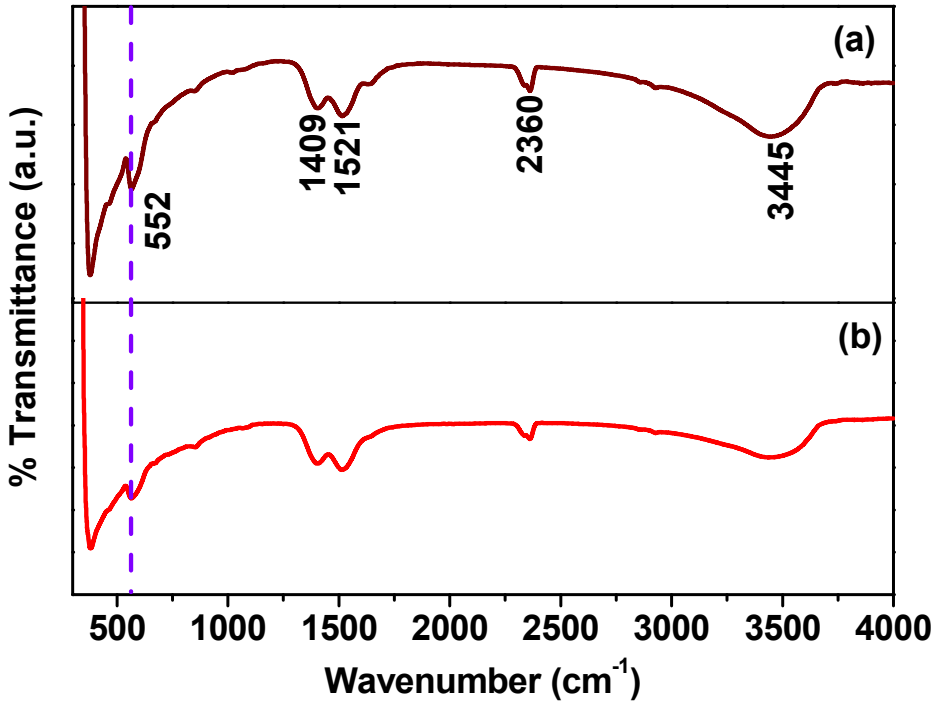

Fig.5. FTIR spectra of Y_2O_3 nanoparticles prepared by using (a) EDTA (b) Na_2-EDTA fuels

The scanning electronmicrographs of Y_2O_3 obtained by EDTA and Na_2-EDTA fuels are shown in Fig. 6a and 6b respectively. The powder obtained using EDTA exhibit highly porous structure with loosely distributed fine particles on the surface; this can be ascribed to lesser solubility of fuel and reduced flame temperature. Whereas micrographs of the powder obtained using Na_2-EDTA fuel shows porous and foamy large aggregates with disconnected structure having significantly large voids. Due to higher solubility of Na_2-EDTA fuel along with $NaNO_3$ acting as in-situ flux high homogeneous combustion occurs. This results in higher flame temperature, which

leads to partial sintering of particles and hence high degree of agglomeration is observed. The above SEM analysis clearly shows difference in the nature of combustion with change in fuel and is consistent with PXRD results.

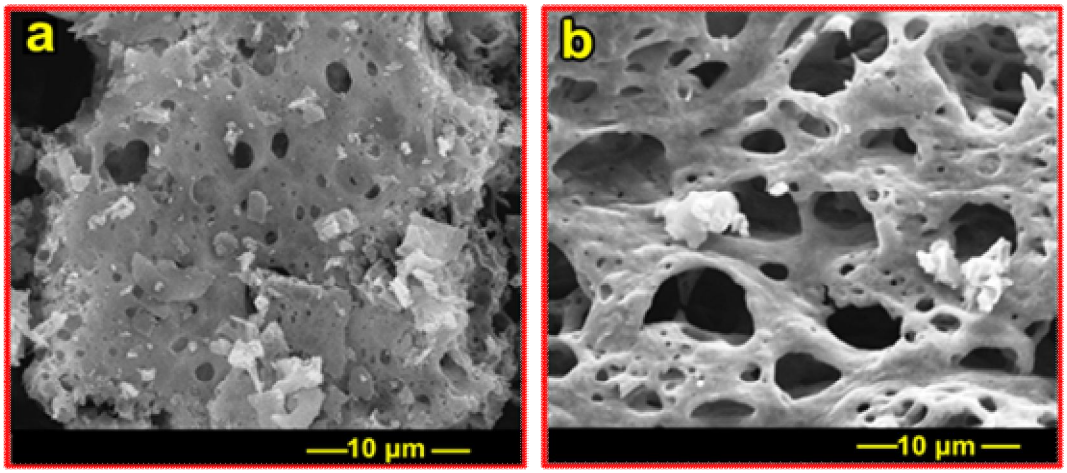

Fig.6. SEM micrographs of Y_2O_3 nanoparticles prepared by using (a) EDTA (b) Na_2-EDTA fuels

Fig. 7a and 7b shows TEM images of Y_2O_3 powders obtained using EDTA and Na_2-EDTA respectively. It can be noticed that nanopowders obtained with EDTA show highly porous frame with high degree of amorphous phase with the particles in the range 10-15 nm. While sample obtained with Na_2-EDTA exhibits highly agglomerated particles with particles in the range 20-50 nm. These results are in consistent with SEM and XRD results.

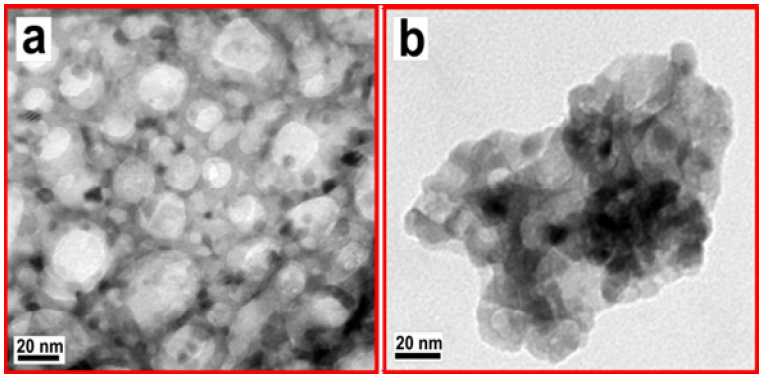

Fig.7. TEM micrographs of Y_2O_3 nanoparticles prepared by using (a) EDTA (b) Na_2-EDTA fuels

The surface area is one of the essential parameters used to characterize powder samples. The surface area (m^2/g) of powder samples is dependent on many other parameters, such as particle size, shape, surface textures, size distribution and open porosity inside a crystalline or in agglomerated particles. Combustion-derived products usually exhibit good surface area as the release of heat (exothermicity) during the combustion reaction is long enough for nucleus formation but too short for grain growth[25]. The surface area and pore size distribution of the samples prepared using EDTA and Na2-EDTA were determined from the corresponding nitrogen adsorption and desorption isotherms, and are presented in Fig. 5(a) and Fig. 6 (b) respectively. The BET surface area of Y_2O_3 powders prepared with EDTA and Na_2-EDTA were 26.99 and 20.11 m^2/g, respectively. This shows that there is substantial change in surface area with change in fuel. The difference in surface area of samples can be attributed to difference in flame temperature and difference in number of moles of gases liberated during combustion with different fuels. The higher surface area for sample prepared with EDTA fuel is due to reduced flame temperature that results in reduced crystallite size. Whereas decrease in surface area for powder prepared using Na_2-EDTA sample is attributed to more homogeneous combustion with higher flame temperature that leads to partial sintering of particles.

Table.3. Comparison of physical parameters obtained from BET analysis for Y_2O_3 nanoparticles prepared by different fuels

System	Surface area (m^2/g)	Pore volume (V) (cm^3/g)	Pore diameter (Å)
Y_2O_3-EDTA fuel	26.5670	0.22249	33.497
Y_2O_3-Na_2-EDTA fuel	20.7758	0.19595	37.726

Fig.8(a) and (b) shows the pore size distribution, which were calculated using the Barrett-Joyner-Halenda (BJH) model from the data of N_2 isotherms. The pore size distribution of the both the samples show that pore diameter 10-160Å with a maximum at about 22 Å, which is in good agreement with SEM observations.

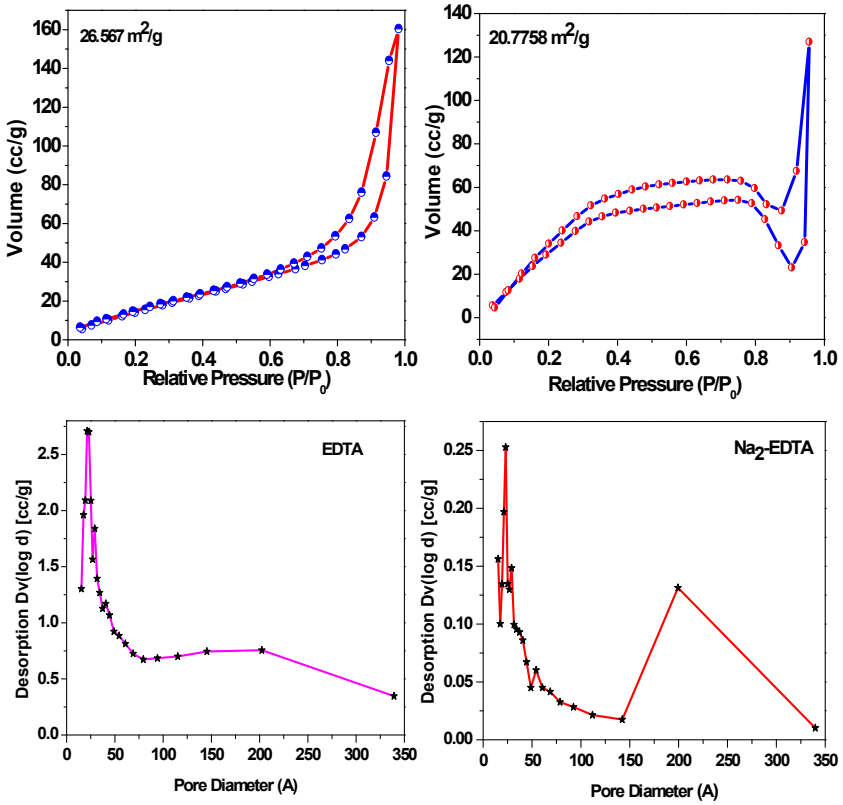

Fig.8. Nitrogen adsorption/desorption isotherms of Y_2O_3 nanoparticles prepared by using (a) EDTA (b) Na_2-EDTA fuels. The BJH pore size distribution curve of Y_2O_3 nanoparticles prepared by using (a) EDTA (b) Na_2-EDTA fuels calculated from the data of N_2 isotherm

The surface area, pore volume and pore diameter for the samples prepared with two different fuels are summarized in Table 2. UV–Vis spectra of Y_2O_3nanoparticles prepared by different fuels are shown in Figs. 9 .Two absorption peaks at ~254 nm (sharp) and ~280 nm (broad) were recorded. The Maximum absorption (~254 nm), can arise due to transition between valence band and conduction band [26]. The weak absorption (~280 nm) in the UV–Vis region is ascribed to transitions involving extrinsic states such as surface traps/defect states/impurities [27]. It is well

known that smaller size particles have high surface to volume ratio. This results in increase of defects distribution on the surface of nanomaterials. Thus the lower is the particle size; nanomaterials exhibit strong and broad absorption bands [28].

The optical band gap energy (Eg) was estimated using Wood andTauc relation [29] given by,

$$(\alpha h\upsilon)\alpha\ (h\upsilon - Eg)^{1/n} \ldots\ldots\ldots\ldots\ldots\ldots \textbf{(2)}$$

where 'a' is the absorption coefficient, hr the photon energy, Egtheenergy gap and n = 2 for direct allowed transition. Eq. (2) for any energycan be rearranged and written in the form

$$(\alpha h\upsilon)^2\alpha\ (h\upsilon - Eg)\ \ldots\ldots\ldots\ldots\ldots\ldots \textbf{(3)}$$

The energy gap is determined by plotting $(\alpha h\upsilon)^2$ versus hυand findingthe intercept on the ht axis by extrapolating the plot to$(\alpha h\upsilon)^2 = 0$ as shown in Figs. 10. The band gap in sample prepared with EDTA is less (Eg= 4.8 eV)when compared tosample prepared with Na2-EDTA (Eg= 5.2 eV).the band gap values (4.8-5.2 eV) well matches with the literature [30].

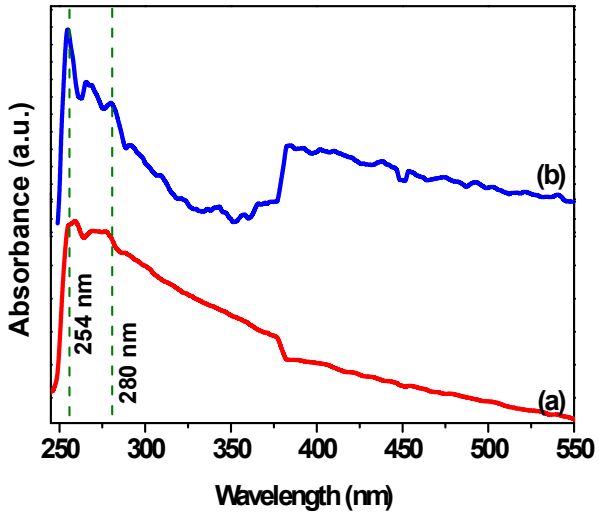

Fig.9. UV–Vis absorption spectra of Y_2O_3 nanoparticles prepared by using (a) EDTA (b) Na_2-EDTA fuels

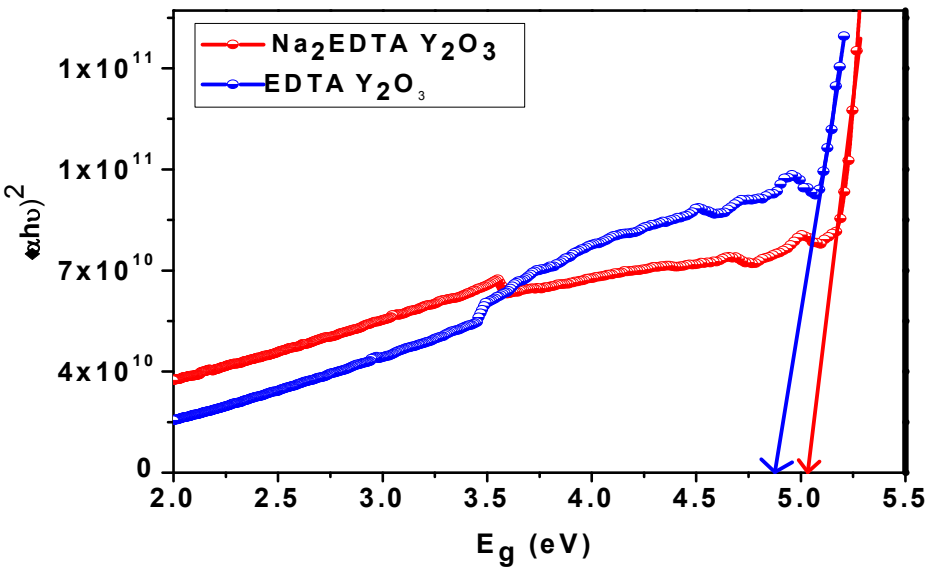

Fig.10. Energy band gap ofY_2O_3 nanoparticles prepared by using (a) EDTA (b) Na_2-EDTA fuels

A probable explanation for the variations observed in the Eg values can be related to the degree of structural order-disorder in the lattice that has direct influence on the intermediate energy levels within the band gap. The optical band gap, Eg values mainly depend on the preparation methods and processing conditions (heat treatment, reaction time, reaction temperature, etc.,). In case of solution combustion synthesis key parameters that can affect the Eg are flame temperature, fuel nature, fuel content and exothermicity etc. In particular these key factors can favour or inhibit the formation of structural defects, which in turn affect the number of intermediate energy levels within the band gap.

In present study, the band gap of the sample prepared using EDTA fuel is less when compared to that prepared using Na_2-EDTA sample. This might be due to the difference in the crystallinity of the sample. Sample prepared with EDTA fuel is slightly amorphous in nature and hence the probability of structural defects is more. While the sample prepared with Na_2-EDTA is highly crystalline and therefore the concentration of structural defects (oxygen vacancies, distortion

or strain in lattice) is reduced, and hence the presence of intermediate energy levels is minimized within the optical band gap and consequently the E_g value increases.

Fig 11(a), (b) and (c) shows the photoluminescence spectrum of Y_2O_3nanophosphors prepare using EDTA and Na_2-EDTA as fuels respectively. Upon 248 nm excitation, a series of emission bands ranging from UV to green region were observed and the bands were centered at 380, 421, 485, 505, 515 and 527 nm. Since Y^{3+} itself is non-luminous and the observed luminescence from Y_2O_3 samples must be related to chemical-bond breakage with resultant carbon formation and / or non-stoichiometry created by the oxygen deficiency in the system [31]. Fig.12 (a) shows the TL glow curves for EDTA, Fig.12 (b) shows the TL glow curves for Na2-EDTA and Fig.12 (c) shows the variation of TL intensity with respective to UV exposure time (min) respectively.We presume Carbon related impurities typically from the fuels used in solution combustion greatly contribute for the luminescence of Y_2O_3. Presence of carbon impurities promotes the formation of the different kinds of defects that are responsible for luminescence**.**

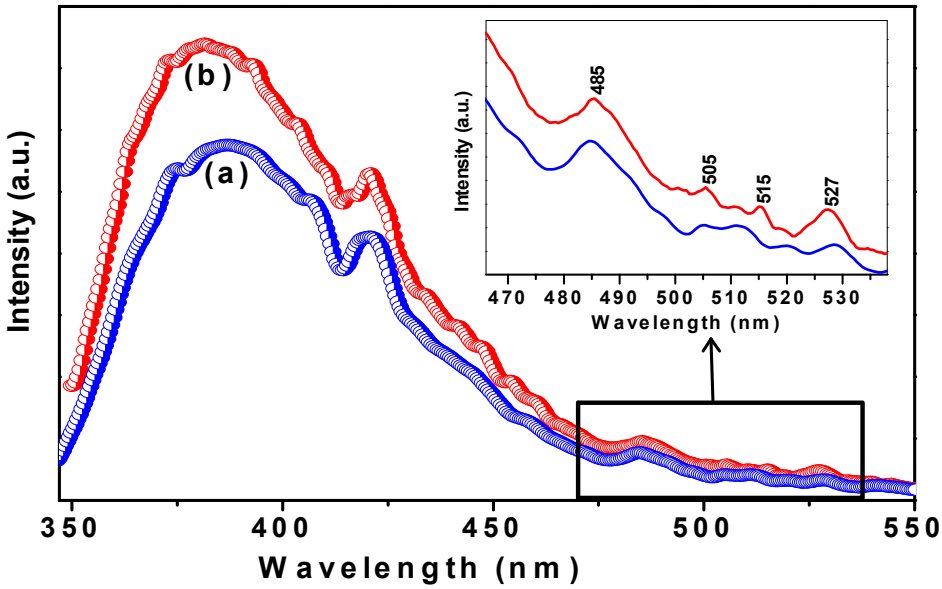

Fig.11.PL emission spectra of Y_2O_3 nanoparticles prepared by using (a) EDTA (b) Na_2-EDTA fuels.

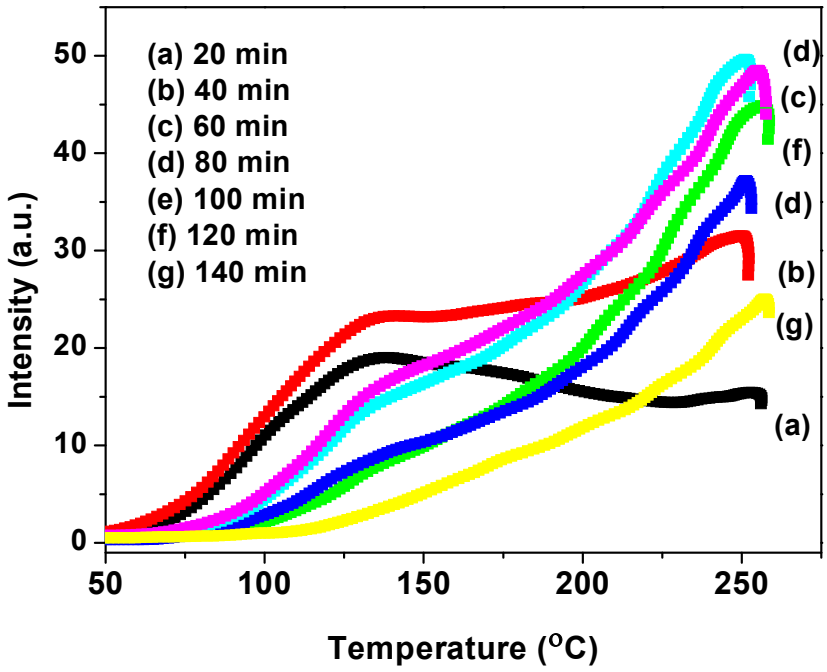

Fig.12. TL glow curves ofUV-irradiated (20–140min) Y2O3 nanoparticles prepared by using EDTA

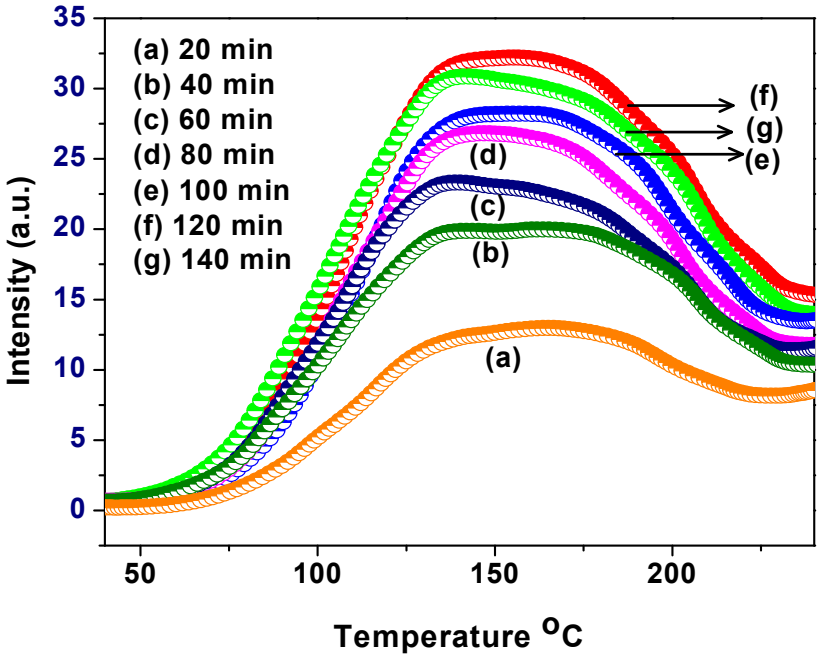

Fig.13. TL glow curves ofUV-irradiated (20–-140min) Y2O3 nanoparticles prepared by using Na_2-EDTA.

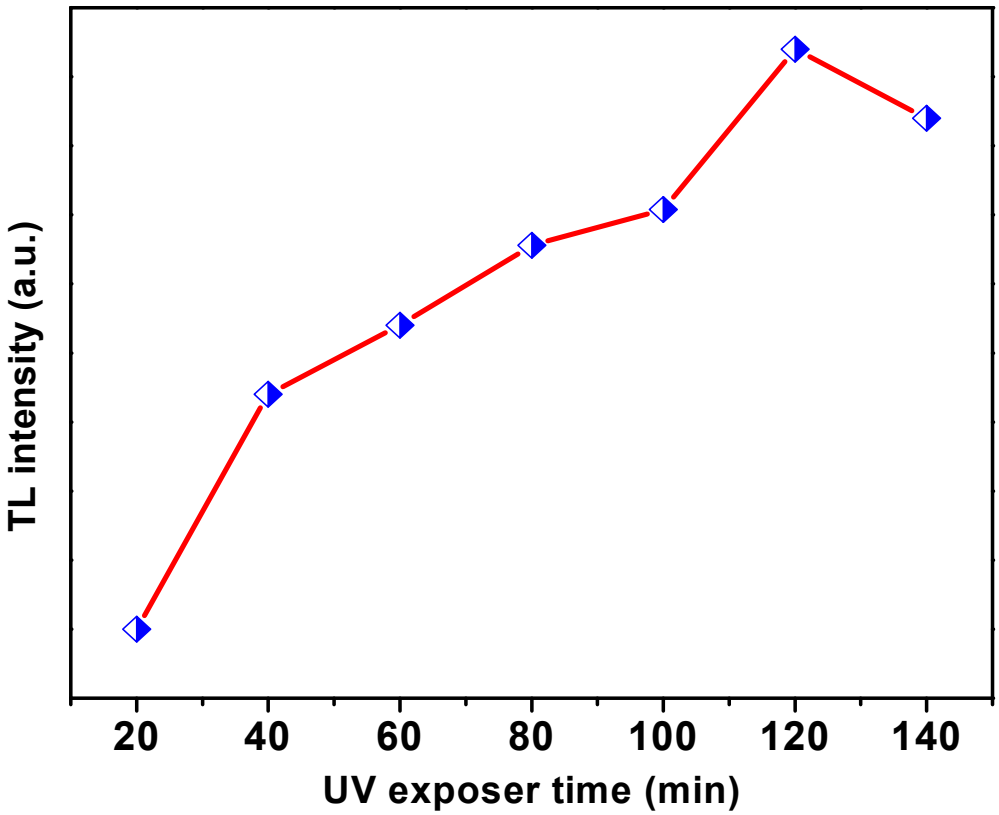

Fig.14. Variation of TL glow peak intensity with UV exposed (10–50min)of Y2O3 nanoparticles preparedwithNa_2-EDTA.

In the emission spectra, the broad emission peak at 380 nm in UV region is attributed to radiative recombination of photo-generated hole with an electron occupying the oxygen vacancy [32]. Emission band centered at 421 nm is observed in both the fuels and is attributed to recombination of a delocalized electron close to the conduction band with a single charged state of surface oxygen vacancy, [33]. The emission band at 480 nm can be attributed to self-trapped excitation luminescence [34]. Other weak emission peaks ~505, 515 and 527 nm are due to different kinds of oxygen vacancies. Further it is observed that the high intense and well resolved emission peaks are recorded for Na_2-EDTA fuel when compared to EDTA fuel. This enhanced photoluminescence response for Na_2-EDTA sample is attributed to the better crystal linty of the sample.

References:

[1] S. Som , S.K. Sharma , S.P. Lochab , Materials Research Bulletin **48** (2013) 844–851.

[2] R.V. Yadav, R.K. Verma, G. Kaur, S.B. Rai, SpectrochimicaActa Part A: Molecular and Biomolecular Spectroscopy **103** (2013) 216–221.

[3] Christopher Waite, Rusty Mann, Anthony L. Diaz, Journal of Solid State Chemistry **198** (2013) 357–363

[4] R. Hari Krishna, B. M. Nagabhushana, H. Nagabhushana, N. Suriya Murthy, S. C. Sharma, C. Shivakumara, and R. P. S. Chakradhar, *J. Phys. Chem. C*, **117 (**2013) 1915−1924.

[5] G.Blasse, B. C. Grabmaier, *Luminescent Materials;* Springer- Verlag: New York, 1994.

[6] G.Blasse, In *Solid State Luminescence*; Katai, A. H., Ed.; Chapman and Hall: London, 1993; p 349.

[7] J. W. Wang, Y. M. Chang, H. C. Chang, S. H. Lin, L. C. L. Huang, X. L. Kong, M. W. Kang, *Chem. Phys. Lett.***405** (2005) 314−317.

[8] P. H. Holloway, T. A.Trottier, B. Abrams, C. Kondoleon, S. L. Jones, J. S. Sebastian, W. J. Thomes, H. Swart, J. Vac. Sci. Technol. B**17** (1999) 758−764.

[9] Wenjing Liu, YuhuaWangn, MingqiZhang,YunxianZheng, Materials Letters **96** (2013) 42–44

[10] Xue-Mei Zhang, Man-Lian Huang, Zhi-Jun Zhang, Bi-Qiu Liu, Jing-Tai Zhao, *Materials Letters*, **68** (2012) 269-272

[11] Qiang Lu, YingJun Wu, AiHua Li , Yang Wang, Yang Gao, HongYanPeng, Materials Science and Engineering B **176** (2011) 1041– 1046

[12] H. J. Eilers, Alloys Compd. 474 (2009) 569−572.

[13] Vijay Singh, Vineet Kumar Rai, Benjamin Voss, Markus Haase, R.P.S. Chakradhar, D. Thirupathi Naidu, Sang Hwan Kim, SpectrochimicaActa Part A: Molecular and Biomolecular

Spectroscopy.**109** (2013) 206-212.

[14] Srirupa T. Mukherjee, V. Sudarsan, P.U. Sastry, A.K. Patra, A.K. Tyagi, Alloys Compd. **519** (2012) 9−14.

[15] Gurvinderjit Singh, V.S. Tiwari, PragyaTiwari, A.K. Srivastava, P.K. Gupta, Alloys Compd. **509** (2011) 4127–4131

[16] M.A. Aghayan, M.A. RodríguezMaterials Science and Engineering C **32** (2012) 2464–2468

[17] R.V. Mangalaraja, J. Mouzon, P. Hedstrom, I. Kero,K.V.S. Ramam, Carlos P. Camurri, M. Oden, journal of materials processing technology **208** (2008) 415–422.

[19] AnuragPandey, Vineet Kumar Rai, RiyaDey, KaushalKumar,Materials Chemistry and Physics.**139** (2013) 483-488.

[21] Yen Pei Fu, J Mater Sci. **42** (2007) 5165-5169

[22] P.Klug, L. E. Alexander, X-Ray Diffraction Procedure; Wiley: New York, 1954.

[23] G. K.Williamson, W. H. Hall, Acta Metall. **1** (1953) 22−31.

[24] S Som and S K Sharma *J. Phys. D: Appl. Phys.***45**(2012) 415102.

[25] B.M. Nagabhushana, R.P.S. Chakradhar, K.P. Ramesh, V. Prasad, C. Shivakumara and G.T. Chandrappa, Philosophical Magazine, **90** (2010) 2009‑2025.

[26] L.K. Pan, Q. Sunchang, C.M. Li, J. Phys. Chem. B **108** (2004)3404–3406.

[27] H.Q. Cao, X.Q. Qiu, B. Luo, Y. Liang, Y.H. Zhang, R.Q. Tan, M.J. Zhao, Q.M. Zhu,Adv. Funct. Mater.**14** (2004) 243–246.

[28] A. Emeline, G.V. Kataeva, A.S. Litke, A.V. Rudakova, V.K. Ryabchuk, N. Serpone,Langmuir**14** (1998) 501–5022.

[29] J.Tauc, In Optical Properties of Solids; Abeles, F., Ed.; North- Holland: Amsterdam, The Netherlands, 1970.

[30] B. N.Lakshminarasappa, J. R. Jayaramaiah, B. M. Nagabhushana, *Powder Technol.***217**(2012)7−10.

[31] E. Kowsari, G. Faraghi, Materials Research Bulletin, **45** (2010) 939-945.

[32] B. Umesha, B. Eraiah, H. Nagabhushana, B.M. Nagabhushana, G. Nagaraja, C.Shivakumara, R.P.S. Chakradhar, J. Alloys Compd. **509** (2011) 1146–1151.

[33] C. Hu, H. Liu, W. Dong, Y. Zhang, G. Bao, C. Lao, Z.L. Wang, Adv. Mater. **19** (2007) 470.

[34] Y. Zhang, K. Han, T. Cheng, Z. Fang, Inorg. Chem. **46** (2007) 4713–4717.

Li^+ co-do pant influence on $Y_2O_3:Eu^{3+}$nanophosphors for red laser applications

1. Introduction

The development of nanophosphors for display applications has developed the interest of researchers. Hence, great efforts have been made to increase the quality, brightness and long term stability of these phosphor materials by various technique [1, 2]. Lanthanide ion doped inorganic host nanophosphors exhibits enhanced luminescent characteristics due to their excellent luminescent properties, better stability in vaccum and absence of corrosive gas emission under electron bombardment when compared to currently used sulfide based phosphors [3, 4].

Ln^{3+} (Eu, Dy, Sm, Tb, Pr, etc) doped Y_2O_3nanophosphors are used as a potential material for display device applications [5-8]. The material having a dimension in the range nano has greater advantages such as reduced electron penetration depth, lower excitation voltages, higher luminescent efficiency, better resolution and large surface to volume ratio has made it better than bulk materials [9]. Among the various lanthanide ions Eu^{3+} trivalent ion provides convenient situation for replacement of A^{2+} sites with isostructural substitution. The red emission by Eu^{3+} ion is due to electric dipole transition $^5D_0 \rightarrow {}^7F_2$ occupying the A^{2+} site without centro-symmetry [10]. Efforts are also made to improve the luminescence efficiency of Eu^{3+} doped oxide nanophosphors by adding co-doped Li^+ ions. Bae et al [11] tried to enhance the luminescent efficiency of $Y_2O_3:Eu^{3+}$ and $(Y, Gd)_2O_3$ by doping it with Li^+ ions. Yeh and Su [12] enhanced the photoluminescence and thermoluminescence properties by doping LiF into Gd_2O_3 due to complete incorporation of Eu_2O_3 into Gd_2O_3 lattice. Shin et al [13] reported the enhancement of cathodoluminescence intensity by the addition of Li^+ co-dopant ions in $Y_2O_3:Eu^{3+}$nanophosphors and its usage in field emission display applications by adding Li^+ co-dopant ions. Jeong et al [14] studied the Li^+ doping effect in enhancing the crystallinity and luminescent brightness of $Y_{2-x}Gd_xO_3$ ceramics. All these studies shows that by doping Li^+ co-dopant ions remarkably affects the crystallinity and luminescence efficiency of the phosphor material.

In addition synthesis also plays an important role in enhancing the material properties. For the development of Li co-doped $Y_2O_3:Eu^{3+}$nanophosphors, environment friendly bio-synthesis

route has been adopted. Many researchers has approached the green synthesis route for the development of oxide nanophosphors by using the extracts of plants such as*neem, alfalfa, Cinnamomumcamphora, emblicaofficinalis, lemon grass, tamarind, Euphorbia tirucalli*, etc [15,16]. Therefore, we have made an approach for the development of Li^+ (1-11 mol%) codoped $Y_2O_3:Eu^{3+}$nanophosphors by using the plant extract of *Aoevera gel* as a fuel in solution combustion technique. The obtained product was further calcined and then subjected to structural and morphological studies. Further, indetail study of photoluminescence (PL) was done and the utilization of these phosphors for display applications.

2. Experimental

$Y_2O_3:Eu^{3+}:Li^+$ (1-11 mol%) nanophosphors was synthesized by green solution combustion technique. For synthesis yttrium nitrate ($Y(NO_3)_3:H_2O$), Europium nitrate ($Eu(NO_3)_3.6H_2O$), Lithium nitrate ($Li(NO_3)_2.2H_2O$) were procured from Sigma Aldrich. *Aleovera gel* extract was collected from the *Aloe vera* plant. The thick gel was diluted by adding 80 ml of double distilled water into 10 ml gel using a magnetic stirrer. For the preparation of $Y_2O_3:Eu^{3+}:Li^+$ (1-11 mol%) nanophosphors, the stiochiometric composition of nitrates were well dissolved in 10 ml of diluted *Aloe vera gel* and mixed well using magnetic stirrer for ~ 5-10 min and then positioned in a preheated muffle furnace maintained at 350 ± 10 ° C. The reaction mixture boils froths and thermally dehydrates forming foam. The entire process was completed in less than 5 min. The obtained product was calcined at 800^{o}C for 3 hr and were further subjected to structural, morphological and photoluminescence studies.

2.1. Instruments used

The formation of $Y_2O_3:Eu^{3+}:Li^+$ (1-11 mol%) nanophosphor was examined by powder X-ray diffractometer (PXRD) (Shimadzu) using Cu-$K_\alpha$radiation (λ=1.54 Å) with a nickel filter was used. The surface morphology of the phosphor was examined by scanning electron microscope (SEM) (Hitachi 3000). Photoluminescence (PL) measurements were carried out using Horiba Fluorolog-3, modular spectrofluoremeter**.**

3. Result and discussions

3.1. Powder X-ray diffraction (PXRD)

The crystallite nature of $Y_2O_3:Eu^{3+}:Li^+$ (1-11 mol%) nanophosphors was studied by recording the PXRD patterns. Fig.1 shows the XRD patterns of $Y_2O_3:Eu^{3+}$ and $Y_2O_3:Eu^{3+}:Li^+$ (1-11 mol%) nanophosphors. The PXRD peaks located at (222), (400), (413), (440) and (622) corresponds to the cubic phase of Y_2O_3 lattice and where in good agreement with the standard JCPDS card no. 70-0134 of yttrium oxide [17]. No impurity peaks related to Eu^{3+}/Li^+ ions were located by varying the concentration of Li^+ ion in $Y_2O_3:Eu^{3+}$nanophosphors. Fig 1(b) shows the enlarged view of highest intense peak (222). From peak it is observed that with increase of Li^+ co-dopant concentration in $Y_2O_3:Eu^{3+}$nanophosphors the peak broadens (FWHM increases) and peak position shifts towards lower angle side. The shift in peak position with Li^+ co-dopant ion concentration in $Y_2O_3:Eu^{3+}$nanophosphors was analyzed by Williamson-Hall plot method [18]. The plots of $\beta\cos\theta$vs $4\sin\theta$ in $Y_2O_3:Eu^{3+}:Li^+$ showed the development of microstrain in the nanophosphors. As Li^+ co-dopant ion concentration increases the microstrain increases. The increase in microstrain results in the shift of PXRD peak position.

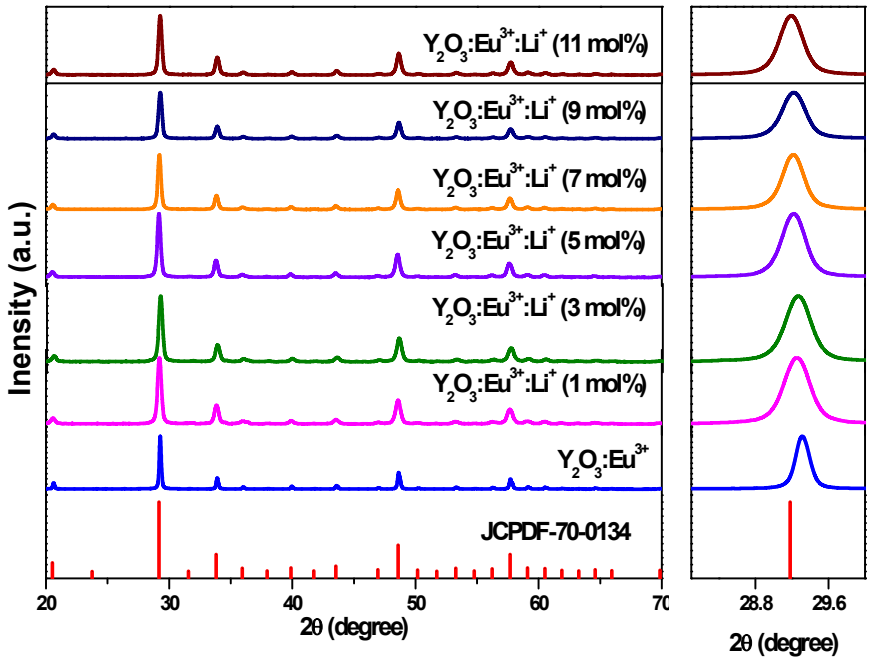

Fig.1. (a) PXRD pattern and (b) enlarged view of intense (222) peak of $Y_2O_3:Eu^{3+}:Li^+$(1-11 mol%) nanophosphors.

Further, particle size was estimated by using Debye Scherrer's formulae, $D = 0.9\lambda / \beta \cos\theta$, where λ is the wavelength of the X-rays, β is the full- width at half maximum (FWHM) and θ is the angle of diffraction [19]. The strain component (ε) present was evaluated by using the relation $\varepsilon = \beta \cos\theta / 4$, and dislocation density (δ) [20] by taking the reciprocal of square of crystallite size ($\delta = 1/D^2$). The stacking fault [21] was estimated by using the relation, $\mathrm{SF} = \left[\frac{2\pi^2}{45\,(3\tan\theta)^{1/2}} \right]$. The estimated crystallite size, microstrain, dislocation density and stacking fault are given in Table.1. From Table.1 it is observed that there was a small variation in the estimated values of crystallite size. The small variation in the crystallite size could be due to negligence of strain component in Debye Scherrer's formulae.

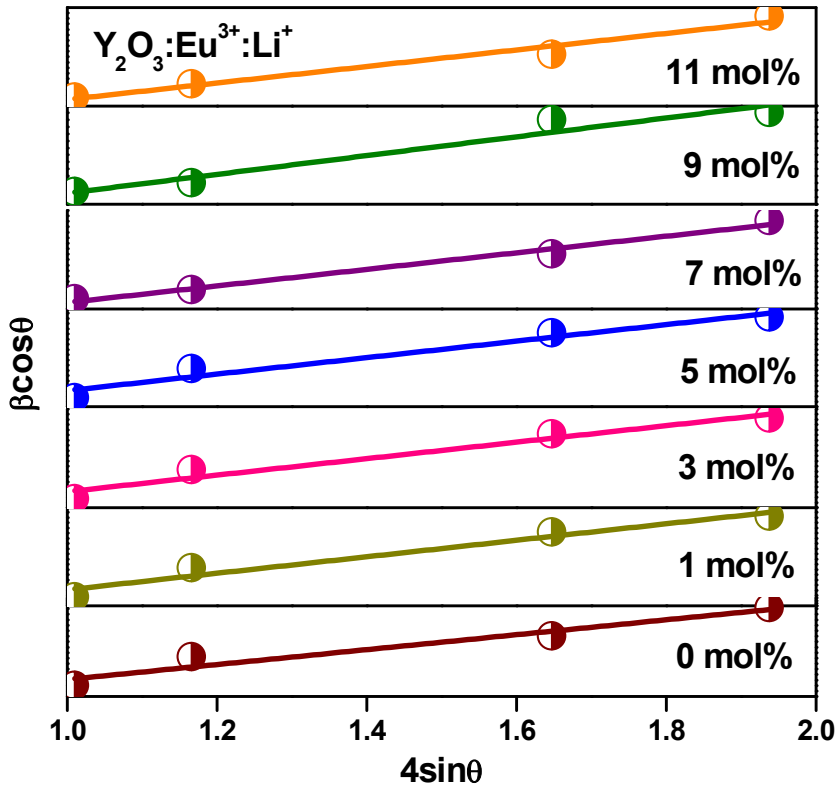

Fig.2. Williamson Hall plots of $Y_2O_3:Eu^{3+}:Li^{+}$(1-11 mol%) nanophosphors.

Table.1. The average particle size and strain parameters of $Y_2O_3:Eu^{3+}$: Li^+(0-11 mol%) nanophosphors.

Li^+ conc. (mol%)	Particle size (nm)		Micro strain ε (10^{-3} $lin^{-2}m^{-4}$)	Lattice strain ϵ ($x10^{-3}$)	Dislocation density δ (10^{18} lin m^{-2})	Stacking fault
	Scherrer's (d)	W-H (D)				
0	7	8	07.5	07.9	1.85	0.496
1	4	8	13.3	11.5	5.80	0.496
3	4	7	13.6	12.2	5.97	0.495
5	4	7	15.1	14.9	5.97	0.495
7	4	6	15.9	15.2	5.51	0.494
9	4	6	15.9	15.6	5.26	0.494
11	4	6	16.1	15.8	4.48	0.494

The structural and cationic distribution in $Y_2O_3:Eu^{3+}:Li^+$ (3 mol%) was estimated by Rietveld refinement (Fig.3). Using Pseudo-Voigt function [22] various parameters such as one scale factor, one zero shifting, four back ground, three cell parameters, five shape, width of the peaks, global thermal factor and two asymmetric factors were fitted. The fitted parameters were in good agreement with the experimentally determined values. The obtained refined values are given in Table.2. Fig.4 shows the packing diagram of $Y_2O_3:Eu^{3+}:Li^+$(3 mol%) nanophosphors which was drawn using diamond software.

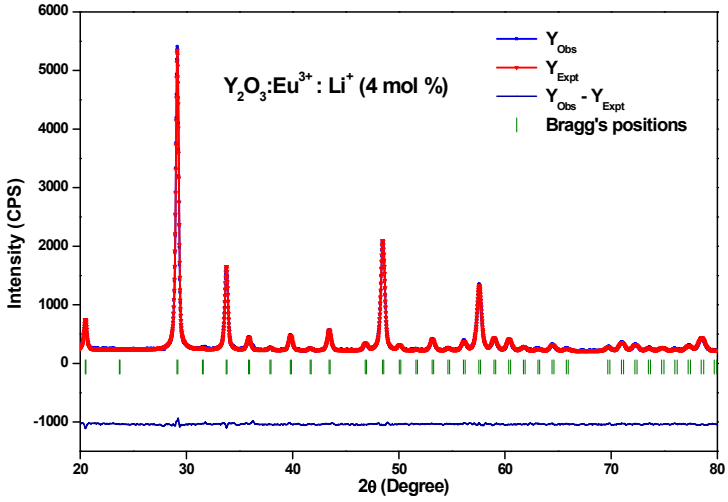

Fig.3. Rietveld refinement of $Y_2O_3:Eu^{3+}:Li^+$(3 mol%) nanophosphors.

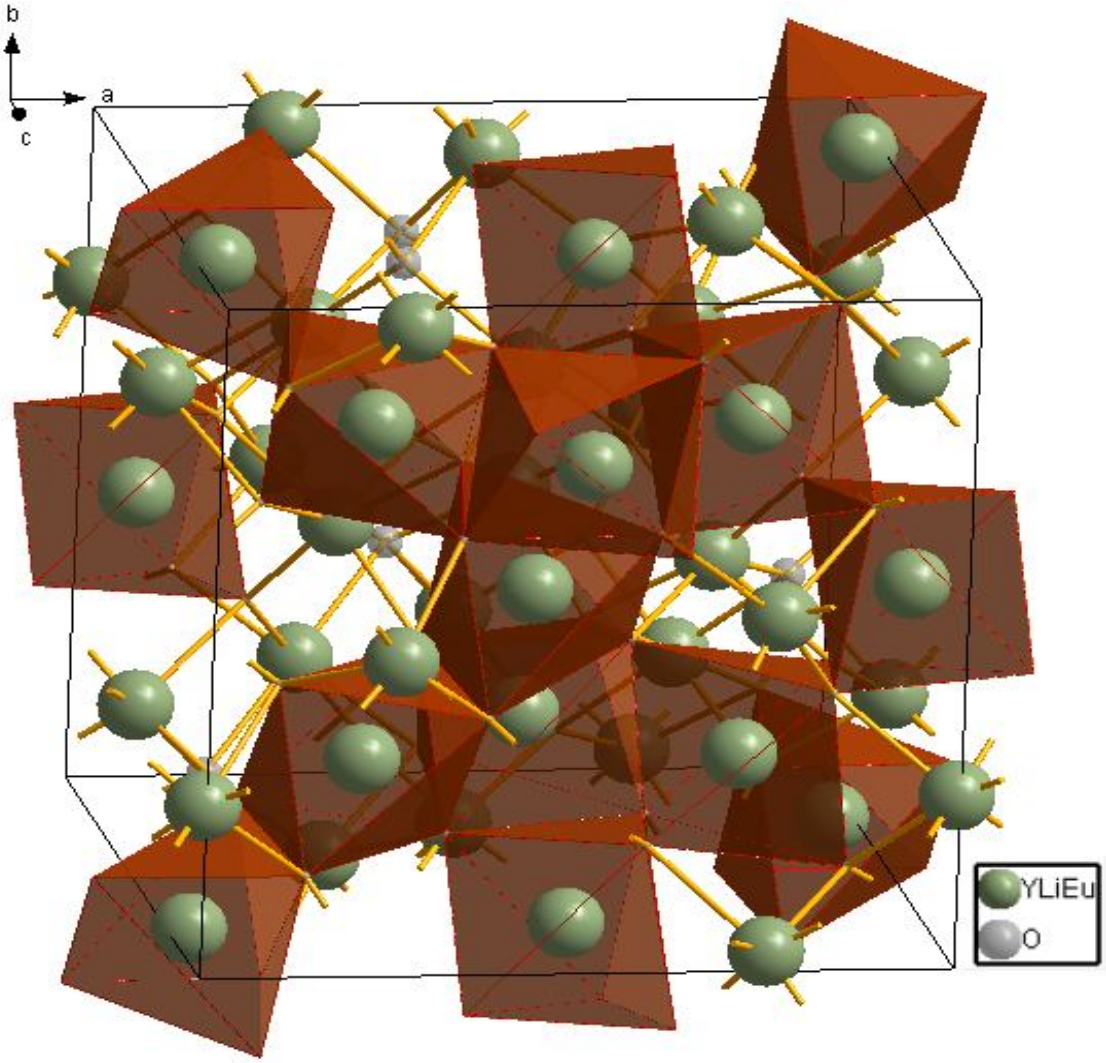

Fig.4. Packing diagram of $Y_2O_3:Eu^{3+}:Li^{+}$(3 mol%) nanophosphors.

Table.2: Rietveld refinement of the Y_2O_3: Eu^{3+}:Li^{+} (0-11 mol%) nanophosphors.

Compounds	**Y_2O_3:** Eu^{3+}	**Y_2O_3:** Eu^{3+} :Li^{1+} (1 mol %)	**Y_2O_3:** Eu^{3+} :Li^{1+} (3 mol %)	**Y_2O_3:** Eu^{3+} :Li^{1+} (5 mol %)	**Y_2O_3:** Eu^{3+} :Li^{1+} (7 mol %)	**Y_2O_3:** Eu^{3+} :Li^{1+} (9 mol %)	**Y_2O_3:** Eu^{3+} :Li^{1+} (11 mol %)
Crystal system	Cubic	Cubic	Cubic	Cubic	Cubic	Cubic	Cubic
Space group	I a -3 (206)	I a -3 (206)	I a -3 (206)	I a -3 (206)	I a -3 (206)	I a -3 (206)	I a -3 (206)
Hall symbol	-I 2b 2c 3	-I 2b 2c 3	-I 2b 2c 3	-I 2b 2c 3	-I 2b 2c 3	-I 2b 2c 3	-I 2b 2c 3
Lattice parameters (Å)							
a = b = c	10.6118	10.6210	10.625	10.6186	10.6168	10.6196	10.6211
$\alpha = \beta = \gamma$	90°	90°	90°	90°	90°	90°	90°
Unit cell volume ($Å^3$)	1194.99	1198.11	1199.46	1197.28	1196.67	1197.64	1198.15
Atomic coordinates							
Y3+							
x	-0.02990	-0.03009	-0.02990	-0.02990	-0.02990	-0.0299	-0.0299
y	*0*	*0*	*0*	*0*	*0*	*0*	0
z	*0.25*	*0.25*	*0.25*	*0.25*	*0.25*	*0.25*	0.25
Occupancy	0.39510	0.50038	0.46242	0.4483	0.45342	0.43951	0.43948
Eu3+							
x	-0.02990	-0.03009	-0.02990	-0.02990	-0.02990	-0.0299	-0.0299
y	*0*	*0*	*0*	*0*	*0*	*0*	0
z	*0.25*	*0.25*	*0.25*	*0.25*	*0.25*	*0.25*	0.25
Occupancy	0.11112	0.11112	0.11112	0.11112	0.11112	0.11112	0.11112
Li+							
x	-------	-0.03009	-0.02990	-0.02990	-0.02990	-0.0299	-0.0299
y	-------	*0*	*0*	*0*	*0*	*0*	0
z	-------	*0.25*	*0.25*	*0.25*	*0.25*	*0.25*	0.25
Occupancy	-------	0.11112	0.11112	0.11112	0.11112	0.11112	0.11112
Y3+							
x	0.25	0.25	0.25	0.25	0.25	0.25	0.25
y	0.25	0.25	0.25	0.25	0.25	0.25	0.25
z	*0.25*	*0.25*	*0.25*	*0.25*	*0.25*	*0.25*	0.25
Occupancy	0.12296	0.16271	0.14452	0.14034	0.15201	*0.14568*	0.14567
Eu3+							
x	0.25	0.25	0.25	0.25	0.25	0.25	0.25

y	0.25	0.25	0.25	0.25	0.25	0.25	0.25
z	*0.25*	*0.25*	*0.25*	*0.25*	*0.25*	*0.25*	0.25
Occupancy	*0.03433*	*0.03433*	*0.03433*	*0.03433*	*0.03433*	*0.03433*	0.03433
Li+							
x	-------	0.25	0.25	0.25	0.25	0.25	0.25
y	-------	0.25	0.25	0.25	0.25	0.25	0.25
z	-------	*0.25*	*0.25*	*0.25*	*0.25*	*0.25*	0.25
Occupancy	------	0.03433	0.03433	0.03433	0.03433	0.03433	0.03433
O2-							
x	1.39261	1.39129	1.39261	1.39261	1.39261	1.39261	1.39261
y	2.34527	2.34371	2.34527	2.34527	2.34527	2.34527	2.34527
z	0.88152	0.87805	0.88152	0.88152	0.88152	0.88152	0.88152
Occupancy	1.11252	1.11261	1.11252	1.11252	1.11252	1.11252	1.01674
Refined Parameters							
R_P	5.02	2.50	1.98	2.30	2.49	2.47	2.51
R_{WP}	7.16	3.61	2.56	2.97	3.28	3.40	3.63
R_{Exp}	4.82	5.71	4.08	4.04	5.64	5.74	5.71
$\chi 2$	2.20	0.400	0.394	0.542	0.338	0.351	0.404
GoF	1.5	0.63	0.63	0.73	0.58	0.59	0.63
R_{Bragg}	3.67	2.58	1.91	2.17	1.88	2.27	0.63
R_F	3.90	2.44	2.17	2.63	2.38	2.78	2.67
X-ray density (g/cc^3)	5.663	5.730	5.496	5.548	5.589	5.617	5.522

3.2. Scanning electron microscope (SEM)

Fig. 5(a-g) shows the SEM micrographs of $Y_2O_3:Eu^{3+}:Li^+$ (0-11 mol%) nanophosphors. Fig (a) shows $Y_2O_3:Eu^{3+}$nanophosphors having fused spherical particles to form a rod like structure. From SEM micrographs it is observed that with increase of Li^+ co-dopant ion the particle size starts to decrease. The decrease in particle size may be due to microstrain created by the addition of co-dopant ion in $Y_2O_3:Eu^{3+}$nanophosphors.

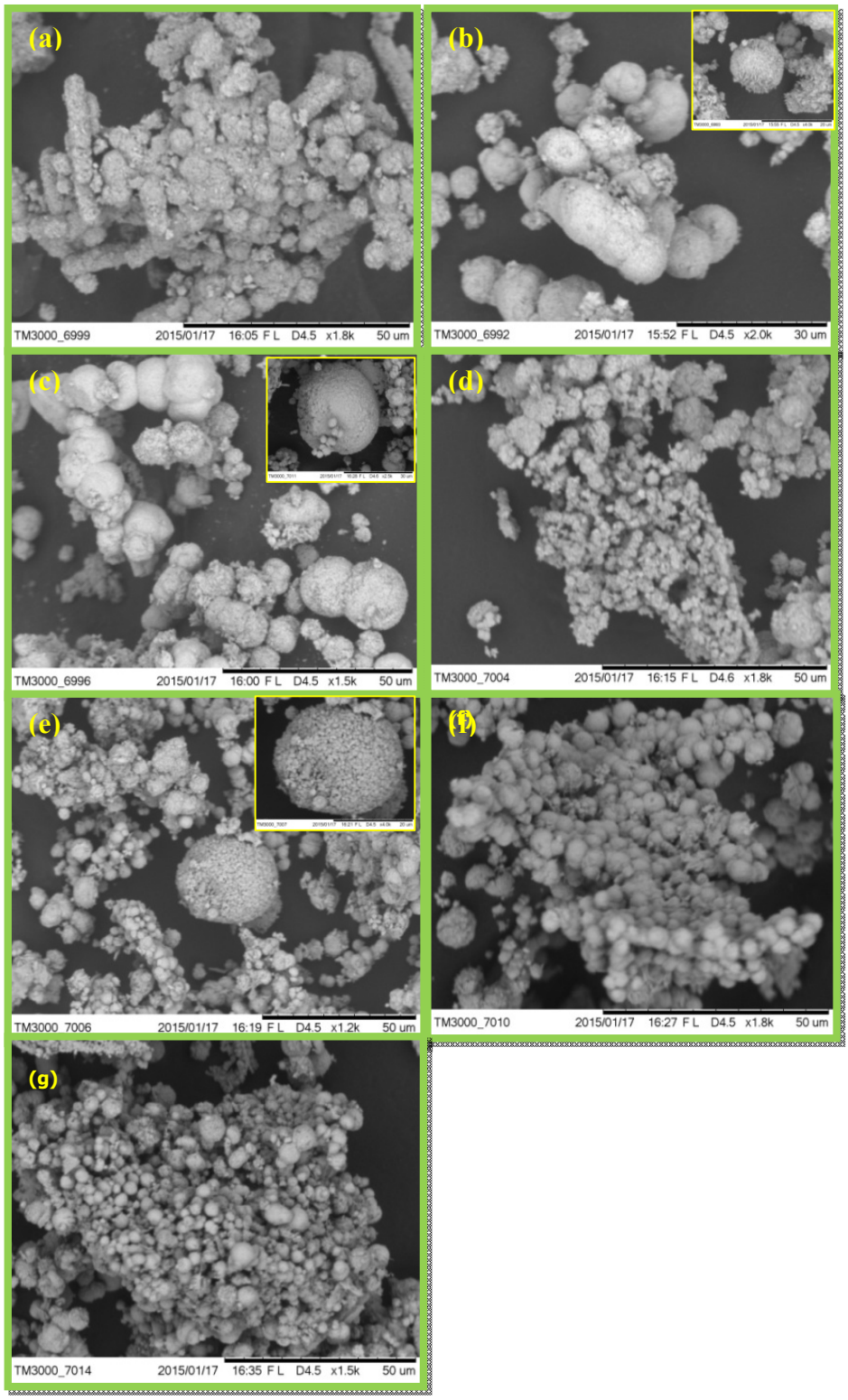

Fig.5. SEM micrographs of Y_2O_3:Eu^{3+}:Li^{+}(0-11 mol%) nanophosphors

Photoluminescence (PL)

The excitation spectra of (3 mol %) Li^+ co-doped $Y_2O_3:Eu^{3+}$nanophosphors was recorded in the range 300-500 nm at an emission wavelength 612 nm is shown in Fig.6. The sharp lines recorded in the range 355-490 nm range are associated with intra-configurational 4f-4f transitions $^7F_0 \rightarrow {}^5D_4$ (364 nm), $^7F_0 \rightarrow {}^5L_6$ (397 nm), $^7F_0 \rightarrow {}^5D_3$ (415 nm) and $^7F_0 \rightarrow {}^5D_2$ (466 nm) transitions of Eu3+ ions in the host lattice site [23, 24]. Fig.7. shows the emission spectra of $Y_2O_3:Eu^{3+}$: Li^+ (3mol%) nanophosphors excited at different excitation wavelengths 364 nm, 383 nm, 397 nm, 415 nm and 466 nm. But emission peaks taken for 415 and 466 nm shows splitting up of 613 nm peak into two spectral lines.

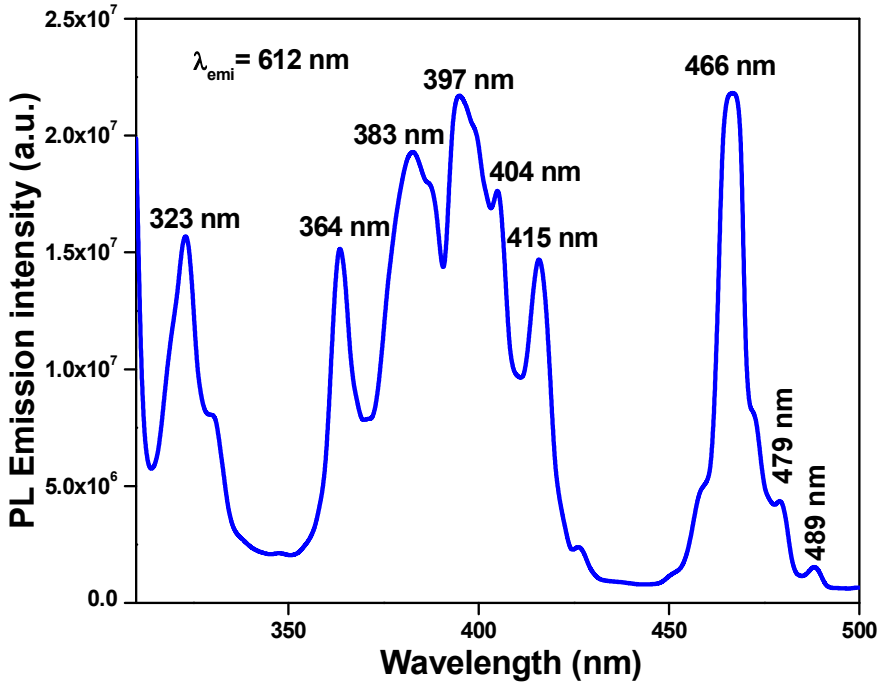

Fig.6. PL emission spectra of $Y_2O_3:Eu^{3+}$: Li^+ (3 mol%) nanophosphors excited at 364, 383, 397, 415 and 466 nmwavelengths.

Further, emission spectrum was taken for different concentration of Li^+ (0-11 mol%) co-dopant ion in $Y_2O_3:Eu^{3+}$nanophosphors at a excitation wavelength of 466 nm as shown in Fig.7. The emission spectrum consists of spectral lines located at 532 and 537 nm (2 spectral lines) corresponding to $^5D_0 \rightarrow {}^7F_0$ transitions, 580-598 nm (4 spectral lines) of $^5D_0 \rightarrow {}^7F_1$ transitions, 609 and 613 nm

(2 spectral lines) to $^5D_0 \rightarrow {}^7F_2$ transitions and 630-662 nm (3 spectral lines) of $^5D_0 \rightarrow {}^7F_3$ transitions and 687-710 nm (4 spectral lines) of $^5D_0 \rightarrow {}^7F_4$ transitions of Eu^{3+} ions in the host lattice [25]. From emission spectra it is observed that the Li^+ co-dopant ions in Y_2O_3:Eu^{3+}nanophosphors has a greater effect on luminescence properties. From Fig.7 it is observed that the emission peak intensity enhances upto 3 mol% of Li^+ ion concentration and with further, increase in Li^+ ion concentration results in splitting up of spectral line at 613 nm into two peaks 609 and 613 nm due to local distortion induced by the co-dopant ion concentration [26].

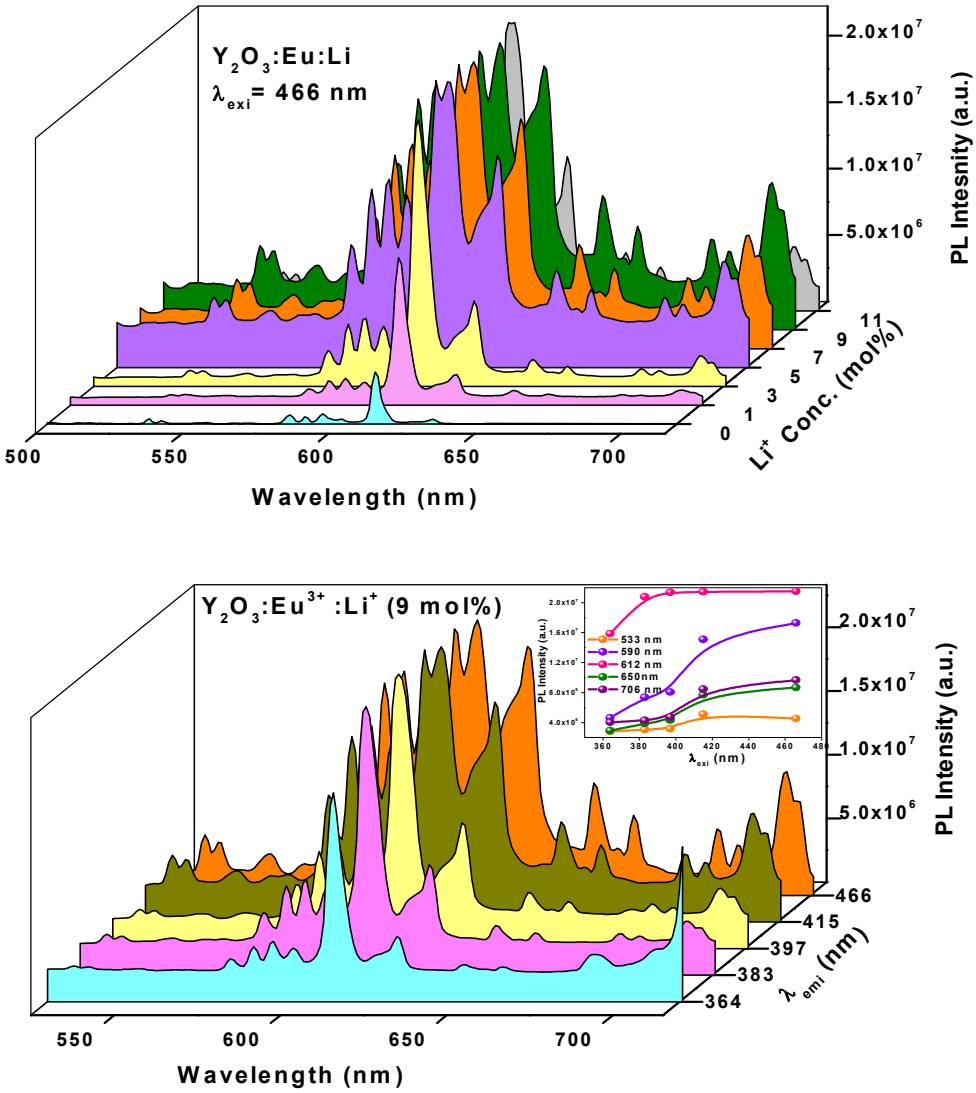

Fig.7. PL emission spectra of Li^+ (0-11 mol%) co-doped Y_2O_3:Eu^{3+}nanophosphors excited at 466 nm wavelength.

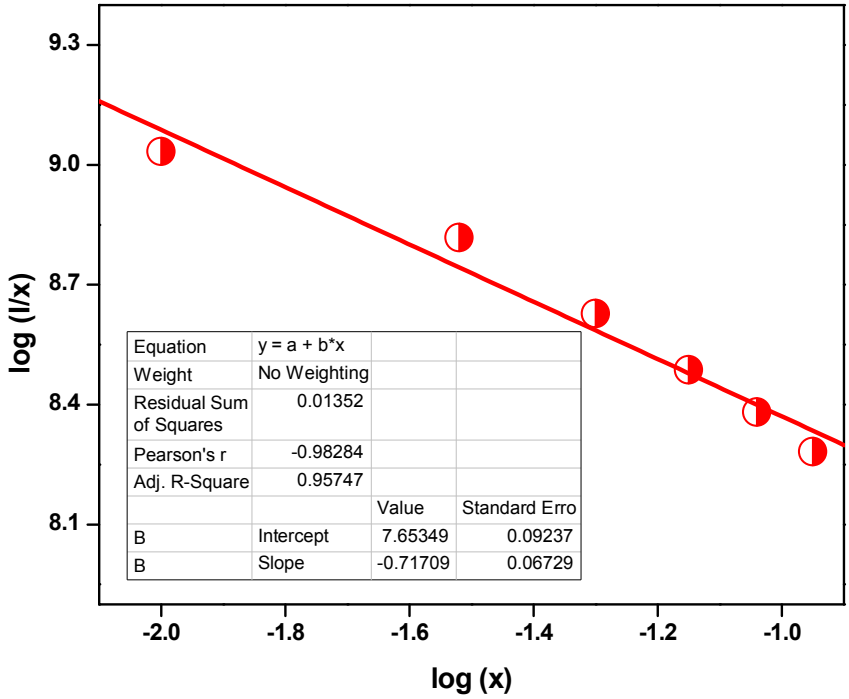

Fig.8. Relation between log(x) and log (I/x) in Li^{+} (0-11 mol%) co-doped Y_2O_3:Eu^{3+}nanophosphors.

Along with splitting up of spectral line with co-dopant ion concentration quenching also takes place. The phenomenon of decrease of intensity at particular concentration is known as concentration quenching. This may be due to energy transfer between the same Eu^{3+} ions in the phosphors. Now, the distance between the two Eu^{3+} ions is estimated by using critical energy transfer distance relation $R_c = 2\left(3V/4\pi N X_c\right)^{1/3}$ where V is the unit cell volume, X_c is the critical concentration and N is the number of crystallographic sites per unit cell [27]. For Y_2O_3:Eu^{3+}:Li^{+}nanophosphors, if R_c value is greater than 5Å the energy transfer between Eu^{3+} ions takes place due to electric multipolar interaction and is estimated by using the following relation

$$\frac{1}{X} = k\left[1+\beta\,(X)^{Q/3}\right]^{-1} \qquad \ldots (1)$$

Where *X* is the concentration of Eu^{3+} ion concentration, *k&β* are constants, *Q* = 6, 8 and 10 for dipole – dipole, dipole – quadrupole and quadrupole – quadrupole interactions [28, 29]. The value of *Q* was resolved by plotting log (*X*) *Vs* log (*I/X*) as shown in Fig.10. From figure we get a linear

graph having intercept 7.653, where Q value is nearly equal to 8, hence it is assumed that quenching takes place due to dipole – quadrupole interactions.

The Judd–Ofelt analysis of the emission spectrum is a powerfultool for evaluating the parity-forbidden electric-dipole radiativetransition rates between the various levels of the rare earth ion [30, 31]. Hence, the site symmetry and luminescence behavior of $Y_2O_3:Eu^{3+}:Li^{+}$nanophosphors was determined by Juddo-Oflet (J-O) intensity parameters Ω_2 and Ω_4, where Ω_4 was the effect of long range and Ω_2 short range which was very sensitive to environment, covalency and structural changes in the vicinity of Eu^{3+} ions. These intensity parameters are very essential in determining the radiation potential of the rare earth ions in Y_2O_3 host lattice and was derived from the absorption spectra. The radiative emission rates and is given by[32].

$$\frac{A_{0\text{-}2,4}}{A_{0\text{-}1}} = \left[\frac{I_{0\text{-}2,4}}{I_{0\text{-}1}}\right]\left[\frac{h\nu_{0\text{-}1}}{h\nu_{0\text{–}2,4}}\right] \qquad \ldots (2)$$

Where $I_{0\text{–}2,4}$is the integrated emission intensity and $h\nu_{0\text{-}J}$ is the energy corresponding to transition $^5D_0 \rightarrow {}^7F_J$ (J = 1, 2, 4). But due to small emission intensity of $^5D_0 \rightarrow {}^7F_0$ and $^5D_0 \rightarrow {}^7F_3$ transitions were neglected. Further, the magnetic-dipole radiative emission rate $A_{0\text{-}1}$ values were found to be ≈50 s^{-1}[32]. The electric dipole radiative emission rates $A_{0\text{-}2,4}$ could be determined by using the following relation

$$A_{0\text{-}2,4} = \frac{64\pi^4(\nu_{0\text{-}2,4})\beta e^2}{3hc^3}\left(\frac{1}{4\pi\pi_0}\right)\chi \sum_{J=2,4}\Omega_J \left\langle {}^5D_0 \left| U^{(J)} \right| {}^7F_J \right\rangle^2 \ldots (3)$$

Where $\chi = n(n^2+2)^2/9$ is the Lorentz local field correction factor and n is the refractive index of host lattice. The $\left\langle {}^5D_0 \left| U^{(J)} \right| {}^7F_2 \right\rangle^2 = 0.0032$ $\left\langle {}^5D_0 \left| U^{(J)} \right| {}^7F_4 \right\rangle^2 = 0.0023$ are non-zero square – reduced matrix elements [33]. Thus by using equation (3), intensity parameters Ω_2 and Ω_4 are evaluated and given in Table.3.

Further, by utilizing the J-O intensity parameters some of the radiative parameters such as transition probabilities, radiative life time, branching ratio, stimulated emission parameters are estimated and life time of the excited state for Eu^{3+} ions were determined. The equation to estimate the radiative transition probability is given by

$$A_T(\psi_J) = \sum_{J'} A_{J-J'} \ldots (4)$$

The radiative lifetime $\tau_{rad}(\psi_J)$ and branching ratio $\beta(\psi_J)$ of an excited state in terms of radiative transition probability is given by [34, 35].

$$\tau_{rad}(\psi_J) = \frac{1}{A_T(\psi_J)} \quad \ldots (5)$$

$$\beta(\psi_J) = \frac{A(\psi_J, \psi^1{}_{J^1})}{A_T(\psi_J)} \quad \ldots (6)$$

And stimulated emission crossectionσ_e [36] is evaluated by the following equation

$$\sigma_e(\lambda_P) = \left[\frac{\lambda_P^4}{8\pi c n^2 \Delta\lambda_{e\,ff}}\right] A_{J'-J} \quad \ldots . (7)$$

Whereλ_P is the emission peak wavelength corresponding transitions, c is the velocity of light, $\Delta\lambda_{eff}$ is the effective bandwidth of the emission transition and n is the refractive index of the host lattice. The estimated parameters are given in Table.3 and 4. From table it is observed that the J-O intensity parameters increases, whereas branching ratio and asymmetry ratio (612 nm/590 nm) were found to decrease with increase of Li^+ concentration in $Y_2O_3:Eu^{3+}$nanophosphors. Further, the optical gain ($\sigma_e\tau$) was estimated by taking the product of stimulated emission cross section and radiative life time. The stimulated emission cross section value of $^5D_0 \rightarrow {}^7F_2$ transition is high when compared to other transitions, hence 612 nm emission dominates in Eu^{3+} ion. The product of emission cross section and effective bandwidth of the emission is highly useful in determining the bandwidth of the optical amplifier. Higher the product of these values, better the performance of the amplifier. And it is observed from Table.4 $^5D_0 \rightarrow {}^7F_4$ transitions has maximum bandwidth gain value ~7.15×10^{-28} cm^3. And also, the product of radiative life time and stimulated emission cross section has also greater effect on optical amplifier gain [37]. The optical gain value corresponding to $^5D_0 \rightarrow {}^7F_2$ transition of $Y_2O_3:Eu^{3+}:Li^+$ has larger optical gain value. Hence, $^5D_0 \rightarrow {}^7F_2$ transition having high optical gain, which is the required condition of lasing action and therefore it is highly useful for red laser application.

Table.3. J-O parameters of $Y_2O_3:Eu^{3+}:Li^+$(0-11 mol%) nanophosphors.

Li^+ conc. (mol%)	J–O intensity parameters ($\times 10^{-20}$ cm^2)		Transitions	A_T (s^{-1})	τ_{rad} (ms)	β (%)	Asymmetry ratio
	Ω_2	Ω_4					
0	1.02	3.53	$^5D_0 \rightarrow {}^7F_1$ $^5D_0 \rightarrow {}^7F_2$ $^5D_0 \rightarrow {}^7F_4$	232	3.83	19	4.91
1	1.35	4.11	$^5D_0 \rightarrow {}^7F_1$ $^5D_0 \rightarrow {}^7F_2$ $^5D_0 \rightarrow {}^7F_4$	246	4.07	21	5.39
3	1.53	6.60	$^5D_0 \rightarrow {}^7F_1$ $^5D_0 \rightarrow {}^7F_2$ $^5D_0 \rightarrow {}^7F_4$	284	3.52	18	4.79
5	1.11	5.18	$^5D_0 \rightarrow {}^7F_1$ $^5D_0 \rightarrow {}^7F_2$ $^5D_0 \rightarrow {}^7F_4$	209	4.79	16	3.94
7	6.31	5.80	$^5D_0 \rightarrow {}^7F_1$ $^5D_0 \rightarrow {}^7F_2$ $^5D_0 \rightarrow {}^7F_4$	200	7.77	09	2.23
9	4.46	6.59	$^5D_0 \rightarrow {}^7F_1$ $^5D_0 \rightarrow {}^7F_2$ $^5D_0 \rightarrow {}^7F_4$	198	1.00	08	1.58
11	3.39	7.01	$^5D_0 \rightarrow {}^7F_1$ $^5D_0 \rightarrow {}^7F_2$ $^5D_0 \rightarrow {}^7F_4$	180	1.20	06	1.20

Table.4. Estimated transition probabilities, radiative life time, branching ratio and stimulated emission parameters of $Y_2O_3:Eu^{3+}:Li^+$(0-11 mol%) nanophosphors.

Li^+ conc. (mol%)	Transition	Δ_{eff} (nm)	σ_e (10^{-22} cm^2)	$\sigma_e x \Delta_{eff}$ (10^{-28} cm^3)	$\sigma_e x \tau_{rad}$ (10^{-25} $cm^2 s^{-1}$)
0	$^5D_0 \rightarrow {}^7F_0$	2	6.83	1.37	2.78
	$^5D_0 \rightarrow {}^7F_1$	5	3.16	1.58	1.11
	$^5D_0 \rightarrow {}^7F_2$	3	3.94	1.18	15.28
	$^5D_0 \rightarrow {}^7F_3$	7	1.66	1.16	7.94
	$^5D_0 \rightarrow {}^7F_4$	8	8.94	7.15	6.95
1	$^5D_0 \rightarrow {}^7F_0$	8	1.71	1.37	6.95
	$^5D_0 \rightarrow {}^7F_1$	5	3.16	1.58	1.11
	$^5D_0 \rightarrow {}^7F_2$	6	7.71	4.63	9.26
	$^5D_0 \rightarrow {}^7F_3$	9	1.29	1.16	6.18
	$^5D_0 \rightarrow {}^7F_4$	13	5.50	7.15	4.28
3	$^5D_0 \rightarrow {}^7F_0$	6	2.28	1.37	9.26
	$^5D_0 \rightarrow {}^7F_1$	6	2.63	1.58	9.26
	$^5D_0 \rightarrow {}^7F_2$	6	9.27	5.56	9.26
	$^5D_0 \rightarrow {}^7F_3$	8	1.45	1.16	6.95
	$^5D_0 \rightarrow {}^7F_4$	7	1.02	7.15	7.94
5	$^5D_0 \rightarrow {}^7F_0$	8	1.71	1.37	6.95
	$^5D_0 \rightarrow {}^7F_1$	7	2.26	1.58	7.94
	$^5D_0 \rightarrow {}^7F_2$	9	1.29	1.16	6.18
	$^5D_0 \rightarrow {}^7F_3$	8	1.45	1.16	6.95
	$^5D_0 \rightarrow {}^7F_4$	13	5.50	7.15	4.28
7	$^5D_0 \rightarrow {}^7F_0$	7	1.95	1.37	7.94
	$^5D_0 \rightarrow {}^7F_1$	7	2.26	1.58	7.94
	$^5D_0 \rightarrow {}^7F_2$	9	1.52	1.37	6.18
	$^5D_0 \rightarrow {}^7F_3$	9	1.29	1.16	6.18
	$^5D_0 \rightarrow {}^7F_4$	11	6.50	7.15	5.05
9	$^5D_0 \rightarrow {}^7F_0$	6	2.28	1.37	9.26
	$^5D_0 \rightarrow {}^7F_1$	7	2.26	1.58	7.94
	$^5D_0 \rightarrow {}^7F_2$	12	1.32	1.58	4.63
	$^5D_0 \rightarrow {}^7F_3$	9	1.29	1.16	6.18
	$^5D_0 \rightarrow {}^7F_4$	11	6.50	7.15	5.05
11	$^5D_0 \rightarrow {}^7F_0$	6	2.28	1.37	9.26
	$^5D_0 \rightarrow {}^7F_1$	6	2.63	1.58	9.26

	$^5D_0 \rightarrow {}^7F_2$	12	5.96	7.15	4.63
	$^5D_0 \rightarrow {}^7F_3$	9	1.29	1.16	6.18
	$^5D_0 \rightarrow {}^7F_4$	10	7.15	7.15	5.56

Fig (9a) and (9b) shows the Commission Internationale de L'Eclariage (CIE) and colour correlated temperature (CCT) diagram and its corresponding co-ordinate and temperature values of $Y_2O_3:Eu^{3+}:Li^{+}$(1-11 mol) nanophosphors. Mccamy [34] gave an empirical formulae to determine CCT values and is given by

$$CCT = -437n^3 + 3601n^2 - 6861n + 5514.31 \quad \ldots (8)$$

Where $n=(x-x_e)/(y-y_e)$, $x_e=0.3320$ and $y_e=0.1858$ is the chromaticity empirical value. From Fig (8) and (9) it is observed that the chromaticity co-ordiante values lies in red region and on increasing the Li^{+} concentration in $Y_2O_3:Eu^{3+}$ the co-ordinate values moves towards deep red region and the average CCT value is found to be 1873 K

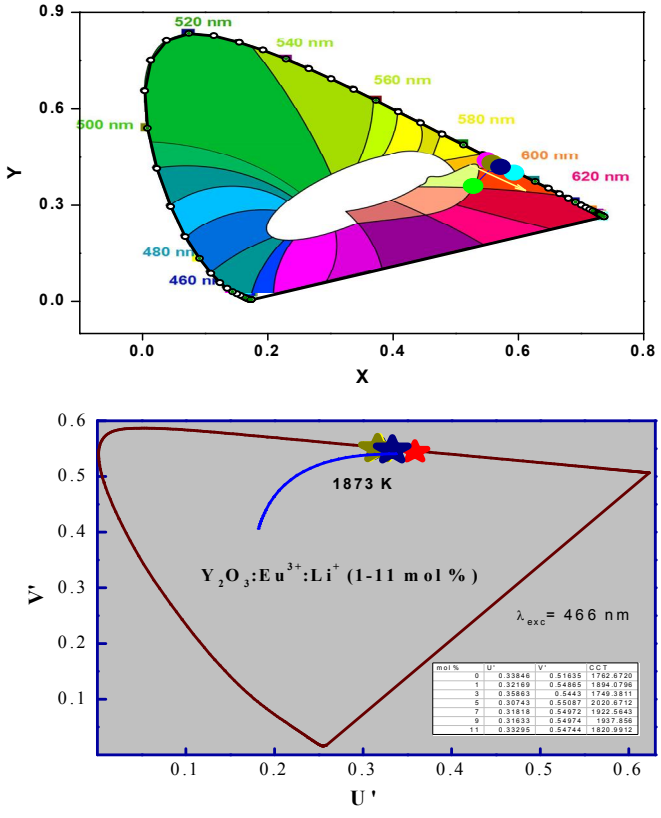

Fig.9. (a) CIE diagram of $Y_2O_3:Eu^{3+}:Li^{+}$(0-11 mol%) nanophosphors.

(b) CCT diagram of $Y_2O_3:Eu^{3+}:Li^{+}$(0-11 mol%) nanophosphors.

Conclusion

Li^+ (0-11 mol%) co-doped $Y_2O_3:Eu^{3+}$nanophosphors was synthesized by low cost, reliable and eco-friendly green solution combustion technique using *Aloevera*gel as a fuel. The PXRD patterns show that there is creation of microstrain with the increase of Li^+ co-dopant concentration in $Y_2O_3:Eu^{3+}$nanophosphors resulting in broadening and shifting of peak position. The particle size estimated by Scherer's method shows that the particle size decreases with increase of co-dopant concentration. This was in good agreement with the particles observed in SEM micrographs. The PL spectra taken for different excitation wavelength showed splitting up of spectral lines due to local distortion induced by the co-do pant ion concentration. The PL spectra of 3 mol% Li^+ ion co-doped $Y_2O_3:Eu^{3+}$nanophosphors showed maximum intensity above which the intensity diminishes due to concentration quenching. The parity-forbidden electric-dipole radiative transition rates were evaluating intensity parameters by J-O analysis. The $^5D_0 \rightarrow {}^7F_2$ transition of $Y_2O_3:Eu^{3+}:Li^+$showedlarger optical gain to value, which was the required condition of lasing action and therefore it is highly useful for red laser application.

References

[1] A. Bergh, G. Craford, A. Duggal, R. Haitz, Phys. Today 54 (2001) 42.

[2] A.H. Narendran, M.A. Petruska, M. Achermann, D.J. Webber, E.A. Akhadov, D.D. Koleske, M.A. Hoffbauer, V.I. Klimov, Nanoletters 5 (2005) 1039.

[3] A. Kitai, Luminescenct Materials and Application, John Wiley & Sons, Ltd., 2008.

[4]R. Bazzi, M. A. Flores, C. Louis, K. Lebbou, W. Zhang, C. Dujardin, S. Roux, B. Mercier, G. Ledoux, E. Bernstein, P. Perriat, O. Tillement. J. Colloid Interface Sci., 273(2004)191.

[5] Y.Q. Li, A.C. Delsing, G. De-With, H.T. Hintzen, Chem. Mater. 17 (2005) 3242–3248.

[6] J.H. Gwak, S.H. Park, J.E. Jang, S.J. Lee, J.E. Jung, J.M. Kim, J. Vac. Sci. Technol., B 18 (2000) 1101–1105.

[7] G. Wakefied, E. Holland, P.J. Dobson, T.L. Hutchison, Adv. Mater 13 (2001) 1557–1560.

[8] H. Jiu, Y. Fu, L. Zhang, Y. Sun, Y. Wang, Opt. Mater. 35 (2012) 141-145.

[9] S. Zeng, K. Tang, T. Li, Z. Liang, J. Colloid and Interface science 316 (2007) 921-929

[10] J.S. Bae, J. of the Korean Phys. Soc. 46(2005)1193-1197.

[11] S.H. Shin, J. H. Kang, D.Y. Jeon, D. S. Zang, J. Lumi., 114 (2005) 275 – 280.

[12] J. H. Jeong, K. S. Shim, H. K. Yang, J. S. Bae, B. K. Moon, S. S. Yi, J. H. Kim, Y. S. Kim, J. Lumi., 122–123 (2007) 87 – 90.

[13] Z. Liu, L. Yu, Q. Wang, Y. Tao, H. Yang, J. Lumin. 131 (2011) 12-16

[14] C. Shang, H. Fan, S, Bu, H. Xia, Y. Du, Chem. Phy. Lett. 577 (2013) 102-106

[15] J. S. Cho, K. M. Yang, Y. C. Kang, Cryst. Eng. Comm. 16(2014) 6170-6174

[16] M. Kabir, M. Ghahari, M. S. Afarani, Ceramics International 40 (2014) 10877 – 10885

[17] J. Zhang, G. Hong, J. Sol. State Chem. 177 (2004) 1292 – 1296

[18] M. Valodkar, P. S. Nagar, R. N. Jadeja, M. C. Thounaojam, R. V. Devkar, S. Thakore, Colloids and Surfaces A: Physicochem. Eng. Aspects 384 (2011) 337 – 344

[19] R. Hari Krishna, B.M. Nagabhushana, H. Nagabhushana, R.P.S. Chakradhar, R. Sivaramakrishna,C. Shivakumara, Tiju Thomas, J. Alloys and Compds. 585 (2014) 129–137.

[20] J. B. Prasanna Kumar, G. Ramgopal, Y. S. Vidya, K. S. Anantharaju, B. Darukaprasad, S. C. Sharma, S. C. Prashantha, H. B. Premkumar, H. Nagabhushana, Spectrochemicaacta Part A, 141 (2015) 149-160.

[21] Y. S. Vidya, K. S. Anantharaju, H. Nagabhushana, S. C. Sharma, H. P. Nagaswarupa, S. C. Prashantha, C. Shivakumara, Danithkumar, SpectrochemicaActa Part A, 135 (2015) 241-251

[22] G.K. Williamson, W.H. Hall, Acta Metall. 1 (1953) 22–31.

[23] Y. S. Vidya, K. Gurushantha, H. Nagabhushana, S. C. Sharma, K. S. Anantharaju, C. Shivakumara, D. Suresh, H. P. Nagaswarupa, S. C. Prashantha, M. R. Anilkumar, J. Alloys Compds. 622 (2015) 86-95.

[24] B.D. Cullity, Elements of X-ray Diffraction, Wesley Addison, 2003, ISBN 0201610914.

[25] K. Gurushantha, K. S. Anantharaju, H. Nagabhushana, S. C. Sharma, Y. S. Vidya, C. Shivakumara, H. P. Nagaswarupa, S. C. Prashantha, M. R. Anilkumar, J. Mol. Cataly. A: Chem. 397 (2015) 36-47.

[26] H.B. Premkumar, H. Nagabhushana, S.C. Sharma, S.C. Prashantha, H.P. Nagaswarupa,B.M. Nagabhushana, R.P.S. Chakradhar, J. Alloys and Compds. 601 (2014) 75–84.

[27] A. Lakshmanan, R.S. Bhaskar, P.C.Thomas, R. Satheesh Kumar, V. Siva Kumar, M.T. Jose, Mats. Letts., 64 (2010) 1809–1812.

[28] M. Xianfeng, W. Yunlong, J. Rare Earths. 29 (2011) 1040

[29] L. Zhou, B. Yan, J. Phys. Chem. Solid 69 (2008) 2877–2882.

[30] G. Chen, H. Liu, H. Liang, G. Somesfalean, Z. Zhang, J. Phys. Chem. C 112 (2008) 12030

[31] G.Y. Chen, H.C. Liu, G. Somesfalean, Y.Q. Sheng, H.J. Liang, Z.G. Zhang, Q. Sun, F.P. Wang, Appl. Phys. Lett. 92 (2008) 113114-1-3

[32] T. Fan, Q. Zhang, Z. Jiang, Opt. Comm. 284 (2011) 249-251

[33] G. Blasse, J. Solid State Chem. 62 (1986) 207–211.

[34] D.L. Dexter, J. Chem. Phys. 21 (1953) 836–850.

[35] S.S. Yao, L.H. Xue, Y.Y. Li, Y. You, Y.W. Yan, Appl. Phys. B. 96 (2009) 39–49.

[36] B.R. Judd, Phys. Rev. 127 (1962) 750-761.

[37] G.S. Ofelt, J. Chem. Phys. 37 (1962) 511-520.

[38] N. Rakov, D.F. Amaral, R.B. Guimaraes, G.S. Maciel, J. Appl. Phys. 108 (2010) 073501-073506.

[39] T.A. Singanahally, S.M. Alexander, Curr. Opin.Solid State Mater. Sci. 12 (2008) 44-50.

[40]B. J. Chen, E. Y. B. Pun, H. Lin, J. Alloys Compd. 479 (2009) 352–356

[41] S. K. Sharma, S. Som, A. K. kunti, J. Lumin. 159 (2015) 317-324

[42] C. S. McCamy, Color Res. Appl. 17 (1992) 142